IN-SITU MONITORING OF SEA ICE DIELECTRIC PROPERTIES AND IMPLICATIONS FOR THE TRACKING OF SEASONAL EVOLUTION OF MICROSTRUCTURE

By

Megan O'Sadnick

RECOMMENDED:

Dr. Erin Pettit

Dr. Martin Truffer

Dr. Hajo Eicken
Advisory Committee Chair

Dr. Paul McCarthy
Chair, Department of Geosciences

APPROVED:

Dr. Paul Layer
Dean, College of Natural Science and Mathematics

Dr. John Eichelberger
Dean of the Graduate School

14 July 2015
Date

IN-SITU MONITORING OF SEA ICE DIELECTRIC PROPERTIES AND IMPLICATIONS FOR THE TRACKING OF SEASONAL EVOLUTION OF MICROSTRUCTURE

A

THESIS

Presented to the Faculty

of the University of Alaska Fairbanks

in Partial Fulfillment of the Requirements

for the Degree of

MASTER OF SCIENCE

By

Megan O'Sadnick, B.A.

Fairbanks, AK

August 2015

Abstract

The microstructure of sea ice evolves throughout the seasonal cycle, from ice formation in the fall through melt in the summer. Observations of this seasonal evolution and its effect on the interaction between sea ice and the surrounding environment face fundamental challenges, however. Any removal of ice cores to obtain data on ice properties results in the loss of brine and alterations of microstructure. The remoteness of field sites also limits observations. Methods to monitor sea ice microstructure continuously and non-destructively are therefore being explored. This thesis examines the potential for the electric properties of sea ice, highly sensitive to the brine distribution within the ice, to serve as a proxy for microstructure and hence other ice transport properties. Throughout the Spring of 2013 and 2014, measurements of low frequency complex dielectric permittivity in the range of 10 Hz to 95 kHz were made in landfast ice off the coast of Barrow, Alaska. Temperature and salinity measurements and ice samples were collected for ice microstructure characterization. Results reveal a significant correlation between measurements of complex dielectric permittivity, brine volume fraction, and microstructural characteristics including pore volume and connectivity. The influence of temperature and salinity variations and further explanation of the relationships between ice properties, microstructural characteristics, and dielectric behavior are explored through multivariate analysis of the combined data set. The findings are discussed in terms of future research directions and promising approaches for *in-situ* ice property monitoring based on dielectric measurements.

Acknowledgements

I would like to first thank Hajo Eicken and Malcolm Ingham for their great amount of guidance and support as I undertook the thesis research summarized therein. Thank you to the Sea Ice group at University of Alaska Fairbanks including Andy Mahoney and Mette Kaufman for help in the field and laboratory, Josh Jones for providing ice temperature measurements and acting as a field assistant when needed, Marc Oggier for being my partner in microstructural research, and Oliver Dammann and Alex Sacco for inspiring conversation both related and unrelated to sea ice. In addition, I would like to thank Erin Pettit and Martin Truffer for providing useful feedback on my research and thesis.

This work would not have been possible without constant encouragement from family and friends. Thank you to my parents for never saying "No", to my sisters for keeping me grounded, and to my brothers for making me laugh. Thank you to Jason Franklin for being my go-to weekend adventure buddy and many other friends who offered a helping hand when it was most needed.

Lastly, I would like to thank the many mentors I have had throughout my academic career who constantly pushed my limits and inspired my curiosity in the many intricacies of our Earth.

Table of Contents

List of Figures

Page

List of Tables

Page

Chapter 1: Introduction

Throughout a large portion of the year, a constantly evolving layer of sea ice covers our polar oceans. In the Arctic, sea ice extent, defined as the ocean area with at least 15% ice coverage, can range from an average minimum of 6.3 million km^2 in September to 15.5 million km^2 in March. In the Antarctic, the cycle is reversed with an average of 2.9 million km^2 of sea ice present in February increasing to 18.6 million km^2 in September (Fetterer et al., 2002). This layer separating air and water will alter the seascape, damping surface waves, impacting the presence and movement of sea life, and greatly increasing the surface albedo.

In contrast with freshwater ice, sea ice contains brine pores and channels, evolving in size and extent from ice formation through melt (see Table 1). The micro-scale evolution of sea ice greatly impacts its behavior on the macro-scale, governing the thermal and mechanical properties of the ice. The former control the conductive and convective transport of heat while the latter will impact the extent and magnitude of large-scale ice deformation. Both are largely determined by ice brine volume fraction as well as the size, shape and spatial arrangement of pores present within the solid ice matrix (Schwerdtfeger, 1963; Ono, 1968; Weeks and Ackley, 1982). The seasonal evolution of sea ice microstructure can also impact the people and communities, in particular in the Arctic, who often depend on the state of the ice cover. Some await its weakening and melt to gain access to areas ice-covered in winter. Others depend on the presence of sea ice for transport and the access it provides to marine mammals in the subsistence hunt (Arctic Council, 2009). Brine pores also provide biota shelter from larger scavengers present at the ice/ocean interface. Convection throughout the lower layers of ice provides these organisms with the nutrients needed to thrive as ice thickens during the winter. Upon ice melt, biota will be released to form the base of a complex polar eco-system (Gradinger et al., 1992; Krembs et al., 2000). Additionally, ice structure controls the dispersal of pollutants emplaced under the ice such as in the case of an oil spill. Both brine volume fraction and connectivity will play an important role in such scenarios, determining when migration of the oil upward to the ice surface will occur (Karlsson et al., 2011).

Table 1: Overview of sea ice microstructure terminology

	Brine Pore	**Brine Channel**	**Brine Pore Throat**	**Grain Boundary**
Formation	Impurities (sea salt ions) are rejected from the ice matrix into pockets of saline brine. In columnar ice, brine films initially form in between ice lamellae. As ice cools, films will become segmented into individual pores.	Brine movement due largely to convective overturning and hydrostatic pressure gradients.	As ice cools, brine films and channels will narrow creating pinch points that can further narrow fully separating pores. When ice warms, pores will reconnect through the widening of these throats.	In granular ice, the consolidation of individual frazil ice crystals into grease and eventually nilas or grey ice. In columnar ice, delineate between grains with differing c-axis orientation. with crystals growing downwards in size as columnar structure becomes established.
Location	At the junction of ice grains in granular ice. Between ice lamellae in columnar ice.	Can form in columnar and granular ice. Findings inconclusive as to the role of ice lamellae in determining location.	Randomly distributed in granular ice. Between ice lamellae and within channels in cold columnar ice.	At the interface of two ice crystals.
Dimensions	Dependent on temperature. Typically <0.5 mm with a mean closer to 0.25 mm in width (Perovich and Gow, 1996). Vertical length will vary widely with brine films potentially extending throughout large portions of the ice.	Up to several millimeters in diameter (Petrich and Eicken, 2010). Can grow to greater than 1m in length (Pringle et al., 2009).	Varies largely depending on pore and channel diameter. Based on dimensions of each, may range from <0.01 mm to 1 mm .	< 0.005 mm in width (Junge et al., 2002).

Given the great impact of sea ice on its surrounding environment, a thorough understanding of its behavior on both the micro- and macro- scale is vital. Observations of the temporal evolution of sea ice, in particular its microstructure, face a fundamental challenge however. Any removal of ice cores to obtain data on ice properties and microstructure results in the loss of brine and alterations of pore microstructure. Observations of critical transitions in microstructure are also limited by the remoteness of field sites, with sampling campaigns

typically few and far between. Methods to observe ice properties *in situ* and continuously are therefore being explored to provide a continuous, undisturbed record of ice property and microstructural evolution. Promising approaches include the measurement of the dielectric properties of the sea ice. Such measurements are dependent on the quantity and distribution of brine and ice and are sensitive to pore space connectivity. Depending on the state of the ice, these properties will vary greatly, possibly serving as proxies for changes on the microscale.

Research into the electric properties of sea ice and their connection to microstructure was first conducted in the 1970s (Addison, 1969, 1970; Vant et al., 1978; Milton, 1981). While these studies relied on simplistic assumptions about ice microstructure they did assist in summarizing the relevant physical processes contributing to measurements of the real and imaginary parts of dielectric permittivity, ε' and ε'' respectively. In more recent years, focus has been placed primarily on dielectric measurements taken at GHz frequencies given their application to satellite remote sensing and usefulness in monitoring ice salinity and brine volume fraction. Hallikainen and Winebrenner (1992), provide a review of the most significant findings and Ingham et al. (2008) review techniques for high frequency measurements. Arcone et al. (1986), Backstrom and Eicken (2006), and Notz and Grae Worster (2008) offer greater explanation of the relationship between high frequency dielectric measurements and ice properties. As frequency decreases to values less than 100 MHz, dielectric measurements are increasingly sensitive to the distribution, shape, and size of brine pores enclosed in the ice matrix (Morey et al., 1984). The relationship between low frequency measurements and microstructure remains relatively unexplored, however, with the exception of work by Addison (1969) and Addison (1970).

Other studies of the dielectric properties of sea ice separate from studies focused on frequency dependence include a study by Ingham et al. (2008) examining surface resistivity measurements in relationship to microstructural anisotropy in columnar ice. Uncertainties in estimates of ice thickness derived from resistivity measurements were first tied to ice anisotropy and substantial differences in the measurements of horizontal versus vertical resistivity. Building off this finding, cross borehole tomography using two electrode strings was applied to track ice anisotropy and the formation and growth of brine channels more closely. Jones et al., (2010), expanded on Ingham's method, using a DC system and four electrode strings to obtain a 3D view of resistivity within an ice volume. Results show a clear relationship between resistivity measurements, the temperature of the ice, and time of year. Particularly evident is the ability of

electric measurements to track the connectivity of brine pores as the ice nears the percolation threshold. This important transition results in the draining of surface melt ponds, the initiation of sea water convection throughout the ice volume, and a dramatic change in the thermal regime of the ice.

The findings from Jones et al. (2010) were next applied to build a basic structural model of sea ice linking measurements of resistivity and hence conductivity to the connectivity of the sea ice. Jones et al. (2012) were successful at modeling the relative size of the pores and their connectivity over time in relationship to the formation factor (equal to the ratio of bulk resistivity to brine resistivity). In order to match measurements of the formation factor however, the model underestimates ice resistivity. Such a trend indicates greater brine connectivity in both the horizontal and vertical directions due possibly to conduction along ice crystal boundaries, not necessarily connected pores. Jones' approach also simplified the geometry of brine pores and channels, modeling such spaces as cubic structures. An overall more complex microstructure may therefore have also contributed to differences between measured and modeled values of resistivity.

Evident but not extensively explored in these previous studies was an increase in the sensitivity of electrical measurements to variations in sea ice microstructure as frequency decreased. Buchanan et al. (2011) conducted a thorough examination of this topic, the low frequency electric properties of sea ice, focusing on measurements of complex permittivity on lab grown sea ice over a frequency range of 10 Hz to 1000 kHz. Complex permittivity is derived from measurements of impedance and phase and represents the amount of polarization a material undergoes when an electric field is applied. Through applying a broadband regression model to results, estimates of the frequency-independent conduction and bulk material polarization and loss were obtained. Buchanan et al. (2011) went on to speculate that trends in measurements of ε' observed at the lowest frequencies may be due to a build up of charge at the pore/ice interface, termed space charge polarization. This trend and the underlying physics hold potential as a proxy parameter representing the microstructural evolution of the sea ice. Lacking in Buchanan's study, however, were actual measurements of microstructural characteristics, such as the geometry of pore spaces, as temperature increased. In addition, lab grown ice while appropriate to obtain general limits on permittivity of sea ice, does differ from natural sea ice. The former is grown in controlled, uninterrupted conditions leading to a uniform columnar structure. Natural sea ice is

exposed to fluctuations in atmospheric and oceanic conditions, resulting in an increase in the number of factors affecting electrical measurements and possibly causing greater variations in the ice microstructure.

The primary purpose of the following work is to further our understanding of natural sea ice, its microstructure, and methods to monitor its evolution through electrical measurements. Results will contribute to the development of a system to be emplaced in the ice, consistently and nondestructively observing the evolution of sea ice throughout the year leading to a better understanding of sea ice and its impact on large-scale processes present in the polar regions. To explore this topic, the relationship between measurements of complex dielectric properties, ice properties (temperature, salinity and brine volume fraction) and specific aspects of its microstructure must be established. Building on previous findings presented above, the three main objectives of the following research are:

1) Examination of the evolution of low frequency complex impedance measurements of natural ice through the warming season in relation to ice properties including temperature, salinity and brine volume fraction. Focus will be placed on datasets collected at Barrow, Alaska during the 2013 and 2014 field seasons.
2) Microstructural characterization of sea ice samples, gathered in parallel to impedance measurements, through acquisition and analysis of X-Ray microtomography data. Results will be examined in relation to complex impedance measurements.
3) Investigation of the physical mechanisms dominating the frequency dependence and seasonal evolution of complex permittivity, incorporating findings of ice property and microstructural analysis. Potential modeling approaches will also be explored to determine appropriate future steps in research.

Chapter 2: Background and Previous Work

2.1 Formation and Evolution of Sea Ice

Sea ice forms in the fall after the upper water column has reached the freezing point of seawater (–1.86 °C for a salinity of 34 ppt). Under turbulent hydrodynamic conditions, such as in a wave field, mm-sized spicules and platelets of ice form in the water column and aggregate into a thin layer of grease ice across the surface. This layer will continue to thicken through further consolidation of ice crystals, leading to the formation of nilas (<10 cm in thickness) and subsequently a solid sheet of young ice (Petrich and Eicken, 2010). The texture of the upper layer is characterized by random crystal orientation. Termed granular ice, it typically makes up the upper 0.20-0.30m of the ice, depending on atmospheric and oceanic conditions (Fig. 1).

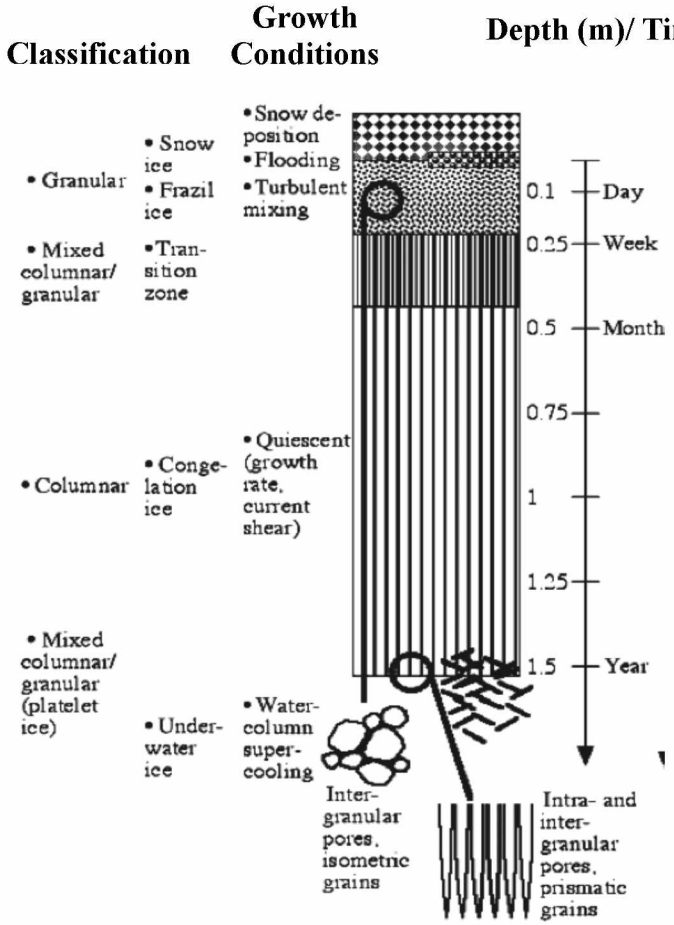

Fig. 1: Ice texture, growth conditions, and timescales of first-year sea ice (Petrich and Eicken, 2010).

Once a surface layer is established, calmer conditions will exist at the ice-ocean interface allowing for the quiescent growth of ice downward. As this occurs, salt ions will be rejected from the ice matrix forming a layer of slightly higher salinity than that of typical seawater at the advancing ice front (described further below). To maintain thermodynamic equilibrium, the interface must retain a temperature equal to the freezing/melting point. Given the higher salinity of this layer, it will be super-cooled with a temperature lower than that of the surrounding ocean. Although heat is primarily conducted upwards away from the ice-ocean interface, this super-cooled layer will also act as a heat sink providing the crystals first to jut through its boundaries a growth advantage. As this process occurs, the structure of the ice will become more uniform, controlled by the molecular structure of ice (Fig.1). Growth occurs preferentially along the basal plane, perpendicular to the c-axis, therefore as ice thickens crystals with the basal plane oriented vertically will outgrow those with differing alignment (Worster and Wettlaufer, 1997). This process, termed geometric selection and accelerated by the presence of the supercooled layer, creates a transition zone from granular to columnar ice. The latter is characterized by the strong vertical orientation of the basal plane of ice crystals, referred to as ice lamellae in the following. These lamellae will become aligned perpendicular, having a c-axis parallel, to the prevailing current allowing for greater transport of salt ions away from the interface (Langhorne and Robinson, 1986).

In between ice lamellae, thin layers of brine will be present, often referred to as brine films. The thickness of these films is controlled by the initial growth conditions with a slower rate of growth leading to greater width. At the very bottom of the ice, these films remain well connected, the result of the relatively warm temperature of the ocean and turbulent conditions. As the distance from the ice/ocean interface increases, portions of these films will become closed off during the winter months, forming brine pores and decreasing the overall brine volume fraction (Petrich and Eicken, 2010). Once temperatures begin to warm, many of these pores will reconnect.

Throughout the winter, ice will thicken as heat is released at the ice/ocean interface and conducted upwards to the surface. The rate at which this occurs depends on weather conditions, snow and ice thickness and the thermal properties of the ice. The latter largely depends on the distribution of brine within ice given the differing thermal conductivity and specific heat capacities of each. Ice growth can therefore be approximated based on derived values of brine

volume fraction but will vary year-to-year due to microstructural differences (Schwerdtfeger, 1963; Ono, 1968; Petrich and Eicken, 2010). In Fig. 2, a typical temperature profile is shown as it evolves from winter into the early months of summer. During ice growth, temperature will increase from the cold surface to the bottom of the ice where temperature remains at freezing. Given the high effective specific heat capacity of sea ice daily fluctuations in ice temperature will be largely confined to the upper ice layers. Only through prolonged temperature changes will ice at depth respond. As the season progresses and daily mean air temperature increases, the temperature profile gradient will decrease as surface temperatures near that of the freezing point.

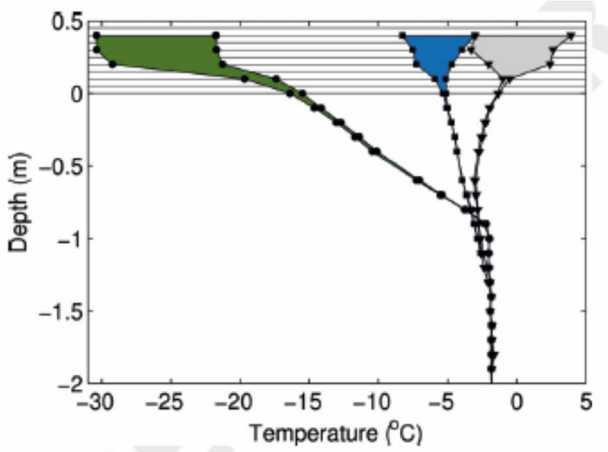

Fig. 2: A typical temperature profile including diurnal fluctuations for Barrow, AK sea ice from mid-February (green), mid-May (blue), and end of May (grey) of 2008. Positive depths represent snow cover (Petrich and Eicken, 2010).

Bulk ice salinity changes with evolving temperatures. As ice thickens, ions rejected from the ice matrix are continuously deposited into the underlying ocean through molecular diffusion, convective overturning and advection through the pore network. These processes result in ice desalination and have strong impacts on both the microstructure of the ice and its related thermal properties. Convective overturning, the primary mechanism for desalination, is driven largely by hydrostatic pressure gradients caused by variations in brine salinity and therefore density (Petrich and Eicken, 2010). In the winter, the upper layers of the ice at the lowest temperature will contain pores holding brine of greater salinity and therefore density than those located nearer to the warmer ice/ocean interface (Fig. 3). The flow of brine downward will increase the bulk salinity of bottom ice layers in addition to increasing porosity and leading to the formation of

brine channels. Upward flow of underlying seawater is responsible for desalination and a resultant decrease in porosity (described further below) (Eide and Martin, 1975)

The resultant salinity profile presented in Fig. 3, is representative of these processes combined with the microstructural evolution that occurs in parallel. Low ice temperatures in the upper layers lead to lesser values in brine volume fraction and hence permeability. Brine of high density and salinity will therefore not be able to flow downward, remaining trapped in pores leading to greater values of bulk salinity in these regions. As depth increases, bulk salinity is observed to decrease given the presence of established brine channels enabling desalinization and leading to relatively constant values of bulk salinity throughout (Petrich and Eicken, 2010). A decrease in salinity further encourages ice growth causing ice lamellae to thicken and interconnect, closing off brine films, forming pores, and decreasing bulk brine volume fraction.

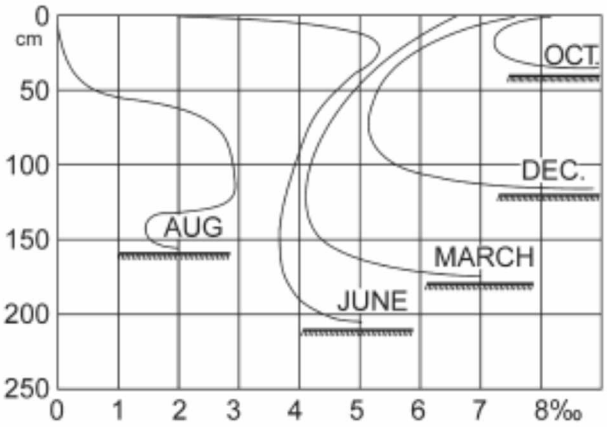

Fig. 3: Seasonal evolution of first-year sea ice salinity profile. Depth is plotted on the y-axis, and salinity in ppt on the x-axis. (Malmgren, 1927).

With spring warming, brine pores will begin to grow in size, connecting, and forming new pathways for brine to flow. This will allow for the redistribution of salinity primarily in the upper layers. During this time, snow and possibly surface melt may be initiated. Until ice reaches a significant permeability, meltwater will pool on the surface sometimes draining downward through the upper layers only to refreeze, forming a layer of superimposed ice. This layer will prevent further drainage downwards even as warming continues, resulting in the formation of pools on the surface. Having an albedo significantly lower than that of surrounding ice, meltwater pools will absorb more radiation and further assist in the warming of the ice (Eicken et

al., 2002). As brine volume fraction continues to increase in parallel to temperature, connectivity between pores will further increase throughout the ice allowing for the transport of both brine and meltwater. Golden et al. (1998) surmise a percolation threshold is present at temperatures above -5°C, salinity is less than 5 ppt, and brine volume fraction is greater than 5% (Golden et al., 1998). Once this threshold is surpassed throughout the depth of the ice, meltwater pooled at the surface will be flushed downward, leading to further desalination. In addition, the flow of meltwater and convection of ocean water will allow for greater transport of heat, assisting in the further deterioration and melt of the ice (Untersteiner, 1968).

At present, the evolution of sea ice microstructure is deduced from core samples extracted from the ice cover or indirectly by tracking in situ ice temperatures and applying crude pore microstructure-temperature models and empirical relationships to derive brine volume fraction (Cox and Weeks, 1983; Leppäranta and Manninen, 1988). This approach is flawed, however, as the removal of an ice core may significantly alter pore microstructure due to brine drainage and changes in sample temperatures. In addition, while brine volume fraction is a useful proxy for a range of ice properties, it does not provide accurate representations of other important microstructural characteristics such as connectivity and the geometry of pore spaces. Development of methods to monitor brine volume fraction and microstructure continuously will therefore lead to a better understanding of the seasonal evolution of sea ice and its impact on surrounding environments.

2.2 The Electric Properties of Ice and Brine

Apparent complex permittivity (ε^*) is calculated from measurements of impedance (I) and phase (φ) by determining the apparent complex resistivity (ρ*) - a measure of a material's opposition of an electric current, and its reciprocal, the apparent complex conductivity (σ*).

(1) $$\rho^* = \rho' + i\rho''$$

(2.1, 2.2) $$\rho' = I * \cos\left(\frac{\pi}{180} * \varphi\right) * G \qquad \rho'' = I * \sin\left(\frac{\pi}{180} * \varphi\right) * G$$

(3) $$\sigma^* = \frac{1}{\rho^*}$$

(4.1, 4.2) $$\sigma' = \frac{\rho'}{\rho'^2+\rho''^2} \qquad \sigma'' = \frac{-\rho''}{\rho'^2+\rho''^2}$$

(5) $$\varepsilon^* = \frac{\sigma^*}{i\omega\epsilon_0}$$

(6.1,6.2) $$\varepsilon' = \frac{\sigma''}{\omega\epsilon_0} \qquad \varepsilon'' = \frac{\sigma'}{\omega\epsilon_0}$$

In Eq. 2.1 and 2.2, G is a geometric factor describing the spacing of electrodes. In Eq. 4, 5.1, and 5.2, ω is angular frequency and ε_0 is the permittivity of free space. Complex dielectric permittivity is a particularly useful property to examine during analysis as it provides a description of how a material interacts with an electric field at a given frequency. The real part of the complex permittivity (ε') defines the amount of polarization a material undergoes while the imaginary part of the complex permittivity (ε'') defines the attenuation, or loss, of energy. The complex dielectric properties of sea ice are influenced by its two main constituents, ice and brine, with contrasting electric properties.

2.2.1 Ice

The electric properties of pure ice are determined by the amount and mobility of defects present in the crystal lattice. Ice-Ih, the form most common on Earth, is characterized by:

1) Two hydrogens adjacent to each oxygen
2) Only one hydrogen atom per bond

Where these conditions are not met in the crystal lattice, a defect is present. These defects enable the movement of protons within the ice and consequently, the transmittance of an electric current (Fig.4).

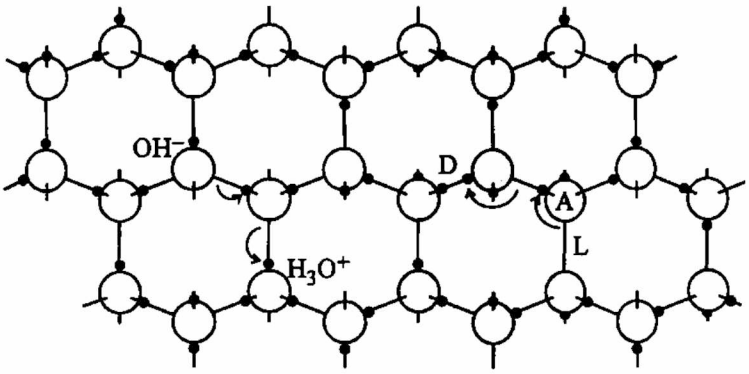

Fig. 4: Schematic of defect types in pure ice. Most common are Bjerrum L- and D- defects shown on the right. Ionic defects, OH^- and H_3O^+ shown to the left, will also impact the electric properties of pure ice (Petrenko and Whitworth, 1999).

The dominant defect in ice is either a site with no protons (Bjerrum L-defect) or a site with two protons (Bjerrum D-defect). Less common are ionic defects with movement of protons along bonds resulting in either a charge surplus (H_3O^+) or deficit (OH^-) (Grimm et al., 2008). Ice temperature greatly influences the movement of defects, with higher temperatures leading to greater mobility and hence polarization. An indicator of the number of defects and mobility is the Debye relaxation time, τ_D, which describes the lag between application of an electric field and polarization. At frequencies longer in period than τ_D, ε' will plateau as it reaches its static permittivity, ε_s, indicating that the material is oscillating synchronously with the electric field (see Table 2). When no DC conductor is present dielectric loss, ε'', will reach a maximum at a frequency of $\frac{1}{\tau_D}$ and decrease down to zero at lower frequencies. If additional conduction mechanisms are present (such as channels within the ice holding brine or air), ε'' will show no maximum. Instead, ε'' will continue to increase with decreasing frequency, the result of conductive loss (Petrenko and Whitworth, 1999). At frequencies larger than τ_D, protonic movement will cease and the real part of the permittivity will be determined only by the displacement of electrons and polarization of individual molecules (Fig. 5). This response will determine the high frequency permittivity, ε_∞ (Table 2).

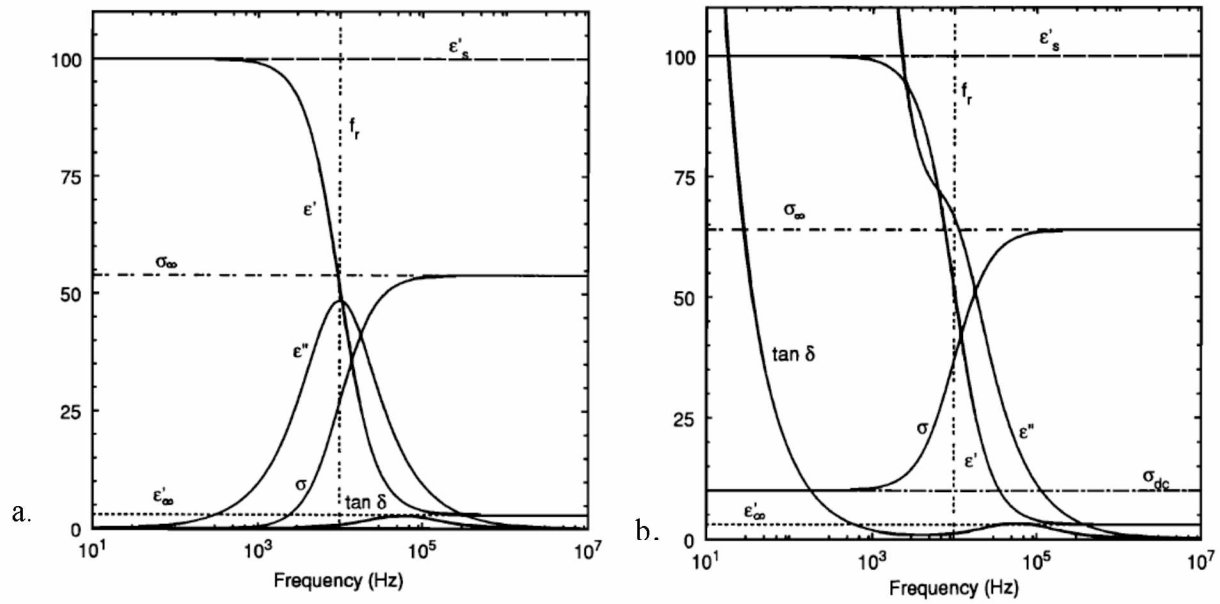

Fig. 5: Comparison of dielectric complex conductivity and permittivity of pure ice (a) and ice with a DC conductor present, i.e. brine channels (b) (Moore and Fujita, 1993). Note the increase in ε'' at frequencies below the relaxation of 10^4 Hz in (b).

Table 2: Values for the static permittivity, high frequency permittivity, and Debye relaxation

	Pure Ice	Pure Water
Static Permittivity (ε_0)	3	6
High Frequency Permittivity (ε_∞)	100	97
Frequency (Hz) of Debye Relaxation	10^4	10^{10}

Grimm et al. (2008) examined the development, structure, and electric properties of saline ice and salt hydrates to better understand ice found in a variety of terrestrial and planetary environments. Mirabilite ($Na_2SO \cdot 10H_2O$,), Ikaite ($CaCO_3 \cdot 6H_2O$), and Hydrohalite ($NaCl \cdot 2H_2O$) are common precipitates in sea ice with their component ions being found in common sea water. When high enough concentrations exist of ions such as Cl^-, they can be incorporated into the ice lattice, their charge balanced by the counterion Na^+ being accommodated interstitially between crystal grains. Grimm et al. (2008) found through complex permittivity measurements in the 10^{-3} to 10^6 Hz frequency range that the dielectric relaxation of doped ice is consistently less than that of pure ice with values being indicative of the type of salt present. Given the higher temperatures of the sea ice examined in this thesis, the dielectric relaxations of doped ice and salt hydrates may be obscured by that of highly conductive brine found in pores and channels. The

findings of Grimm et al. (2008) however, are important in understanding and identifying causes for specific trends seen in measurements of complex permittivity of natural sea ice. In addition to the lab-based study by Grimm et al. (2008) focused on initial ice formation and size distribution of brine channels, greater attention is now placed on connecting key ice properties to electrical measurements to provide a better description of the microstructural evolution of natural sea ice.

2.2.2 Brine

When determining the electric properties of brine, one must first consider those of pure water. Due to the absence of salts, pure H_2O has very low conductivity with current being conducted only through H^+ and OH^- ions. Individual molecules will oscillate in response to the applied electric field, contributing to the magnitude of ε' and ε''. As temperature increases, hydrogen bonds will weaken resulting in a decrease in values of ε'. The magnitude of ε'' will also decrease due to less friction and thus drag present at warmer temperatures. The frequency of the Debye relaxation will increase as warmer temperatures allow the molecule to oscillate at a higher frequency (Fig. 6).

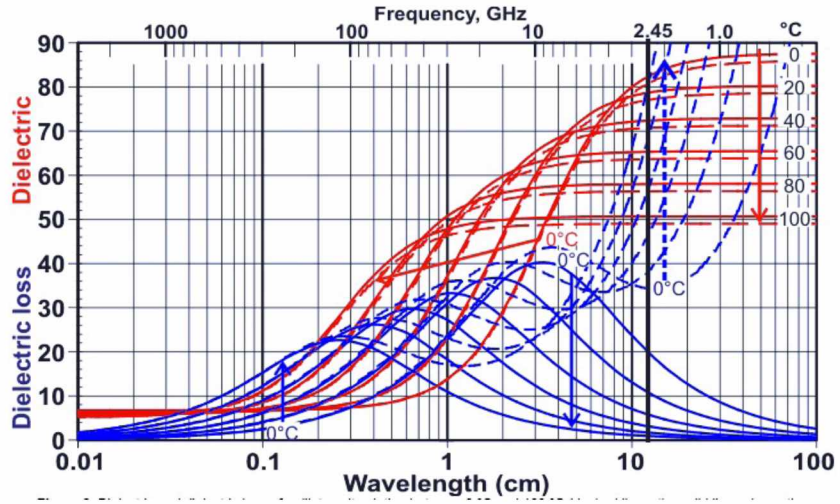

Fig. 6: Variation in the real part, ε' (red), and imaginary part, ε'' (blue), of the complex permittivity for pure water. Arrows point in direction of temperature increase from 0 °C to 100 °C. Dashed line shows electric response of a dilute salt solution. Data is only indicative, not exact (Chaplin, 2014). Note the scale from 1.0 to 1000 GHz, substantially higher than that presented in Fig. 5.

With the addition of salts, conductivity will increase from the movement of additional ions leading to ε'' becoming a measurement of both dielectric as well as conductive loss

(collision of charges). As a result, after an initial drop in magnitude due to the Debye relaxation, ε'' will continue to increase with a decrease in frequency. Measurements of ε' will maintain their general relationship to frequency as salinity increases, showing only a slight decrease in magnitude due to the alignment of H_2O with charged ions as opposed to the actual electric field. The Debye relaxation of a solution also varies with temperature and salinity. An increase in temperature leads to an increase in τ_D and therefore a decrease in the relaxation frequency. Variations in salinity have an opposite but weaker effect, with an increase in the concentration of salt leading to a slight increase in the relaxation frequency (Hasted, 1973).

For this study, measurements were gathered over a frequency range of 10 Hz to 95 kHz thus including the relaxation of ice but far below the relaxation of brine. Measurements of ε' and ε'' of sea ice are expected to deviate substantially from values for brine and pure ice however. Such behavior is caused by interfacial polarization effects at the pore/ice boundary. The magnitude of this impact and the physical processes responsible are not entirely understood, however, and remain a topic of study when examining the electric behavior of porous materials.

2.3 Spectral Induced Polarization

Spectral induced polarization (SIP), a term most commonly used in the field of near-surface geophysics, describes a method whereby an alternating current is applied over a broad range of frequencies and the material's electric response measured. Developed in the past two decades, SIP capitalizes on the presence of interfacial polarization and is often used in the natural resources including mineral and oil deposits (Seigel et al., 2007). Data from measurements of complex dielectric properties available for sea ice show similar frequency dependence as those made on other rocks and minerals.

In the context of resource exploration, SIP research has focused on the dielectric response of metallic minerals, associated surface and polarization effects and relationships to microstructure (Van Voorhis et al., 1973; Pelton et al., 1978). Kemna et al. (2012) provide a thorough review of significant field- and lab-based SIP findings, advancements, and suggestions for future work. Some studies have considered links between permittivity and the hydraulic conductivity of a porous material, including the role of pore throat geometry and size. Scott and Barker (2003) found a strong relationship between the distribution of pore throat diameter and the phase angle of the complex conductivity. The authors attributed this finding to the presence

of an electric double layer, a layer of cations present on all mineral grains. This type of polarization, termed electrochemical, is likely influenced by a material's microstructure and may help explain dielectric permittivity behavior at frequencies below 1000 Hz. Leroy and Revil (2009) conducted a thorough theoretical and experimental examination of the mechanisms responsible for the dielectric response of water saturated packed glass beads. The authors examined both electrochemical and Maxwell-Wagner polarization. The latter is largely responsible for the high frequency response of a composite material and is attributed to an electric field induced by the build-up of free charges at the pore interface. It is often directly related to pore properties in a material. Of particular significance is a potential link between the smoothness of a pore and resultant dielectric behavior. Although sea ice differs from the geo-materials in most SIP studies, Scott and Barker (2003) noted that grains of similar sizes can produce very different frequency spectra depending on pore size distribution and its relation to sediment compaction. For sea ice, pore size, geometry, and connectivity are most relevant in this context and allow for comparisons with past studies cited above.

In describing the SIP frequency dependence, the empirical Cole-Cole model is often applied to derive specific physical properties from SIP measurements (Pelton et al., 1983). In generalized form the frequency dependence of impedance is given:

$$Z(\omega) = R_0(1 - m\left(1 - \frac{1}{(1 + (i\omega\tau)^c)^a}\right))$$

where R_0 is DC resistance, m chargeability, τ Debye relaxation, and c and a are exponents related to pore shape and polarization. Through examination of the Cole-Cole model and its various forms, the Debye relaxation has been linked to the distribution of pore sizes. It is surmised that τ is a reflection of many relaxation times for pores of different size and hence contrasting dielectric behavior superposed (Nordsiek and Weller, 2008). The distribution of these relaxation times can be derived from a Debye Decomposition (DD). Zisser et al. (2010) explored DD and found a potentially strong relationship between effective relaxation times and the permeability of low-porosity sandstone. While the DD approach is still being refined, it holds considerable promise to define specific relationships between SIP data and the physical properties of porous media. For studies of sea ice electric properties, these models offer a tool to analyze complex dielectric measurements and improve their physical interpretation.

Chapter 3: Methods

3.1 Collection of Complex Permittivity Measurements

3.1.1 Sampling Site and Data Collection

The permittivity array and mass balance site were installed approximately 8 km northeast of the NARL-UIC base in Barrow, AK on shorefast sea ice. This location was chosen given the protection from winds and currents offered by a thin strip of land leading to Point Barrow to the East and a grounded pressure ridge to the West. The latter is known to form annually. The undisturbed and stable position of the ice allows for gradual in-situ freezing and a homogeneous structure with lamellae oriented perpendicular to the alongshore current. Little ice deformation will occur in this region, resulting in relatively flat ice topography and consistent snow depth. Before any instruments are emplaced, boreholes are drilled around the prospective area of ice (typically ~25 m^2) to further ensure constant ice thickness and therefore growth conditions (Fig. 7).

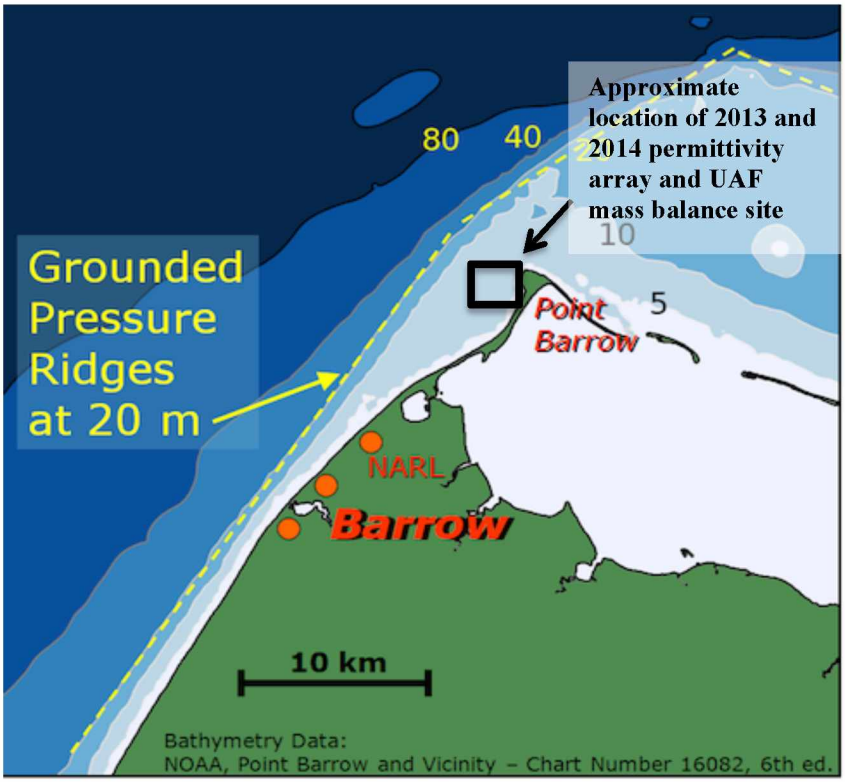

Fig. 7: Map of coastal region at Barrow and approximate water depth. Ice formed between Point Barrow and grounded pressure ridges is well protected allowing for the formation of landfast sea ice ideal for the placement of mass balance site and permittivity array (Petrich, 2012).

The mass balance site is composed of instrumentation to monitor snow depth, ice thickness, air and water temperature (Fig. 8). Ice temperature is also measured using strings of thermistors frozen into the ice in January. Measurements are ideally taken every 15 minutes from January through June and transmitted back to the NARL-UIC base before being transferred to a larger server accessible at University of Alaska Fairbanks thus providing up-to-date measurements of ice conditions (Druckenmiller et al., 2009).

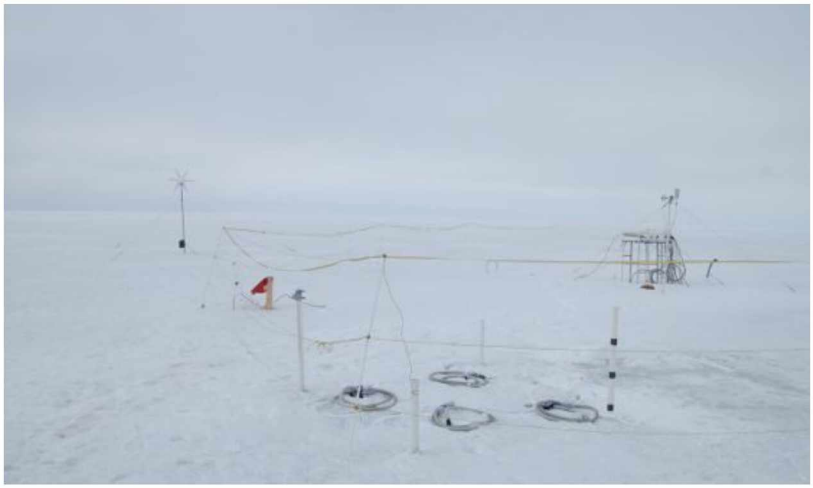

Fig. 8: UAF mass balance site and permittivity array. The latter is composed of the electrode strings shown in Fig. 8 frozen vertically into the ice in a 1x1 m array. The control box is powered by a wind turbine and records measurements of ice thickness, ice temperature, water temperature, air temperature, and snow depth.

The permittivity array was installed within 15 m of the mass balance station and is composed of four electrode strings installed vertically in the sea ice at the corners of a 1 m x 1 m square. Each 2.0 m long string was composed of marine grade stainless steel washers positioned at 0.1 m vertical increments and held in place by epoxy resin (Fig. 9). The strings were placed into boreholes drilled in early January to allow adequate time for ice to regrow before measurements were collected.

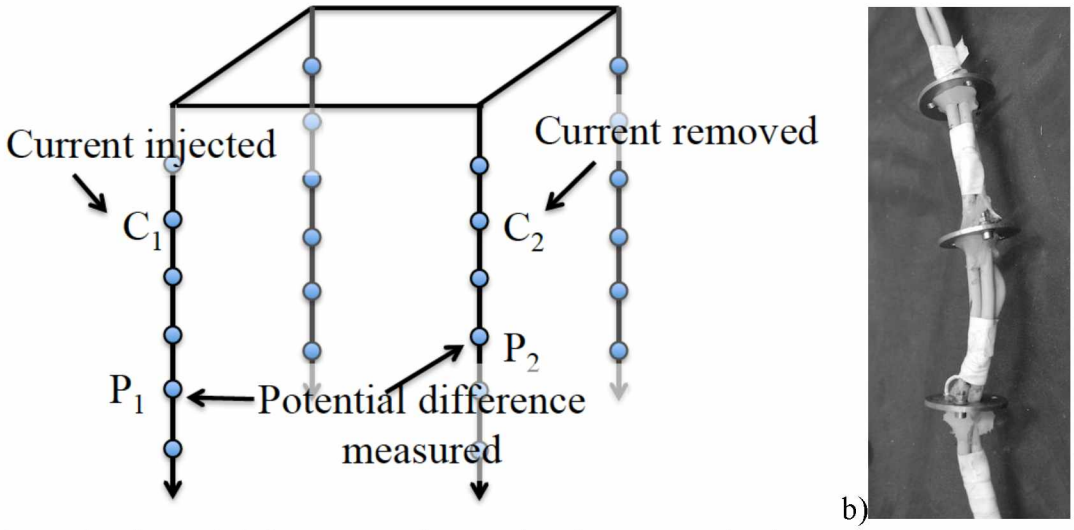

Fig. 9: a) Schematic of permittivity array and example of current and voltage measurement. Each electrode string is 2.0 m long with electrodes placed every 0.1 m b) Photograph showing electrodes composed of marine grade stainless steel, with holes to enhance contact with the ice.

Sampling dates were chosen in an attempt to capture the microstructural evolution of the ice as it undergoes the transition from the cold ice-growth season into spring and summer melt. The first set of measurements was taken in late March, long after the thermal disturbance has subsided and new ice has accreted at the bottom of the ice cover. The second set of measurements in mid-May aimed to capture early warming and the onset of percolation at the surface while the third set, taken in early June, was intended to capture ice after the percolation threshold had been surpassed throughout thus enabling meltwater flushing and desalination.

Measurements of impedance and phase were first gathered through injecting and removing current (I) at two selected electrodes. Voltage was simultaneously measured at two additional electrodes and the potential difference between the two determined (ΔV). Impedance (Z) is defined as the ratio of these two values ($Z = \frac{\Delta V}{I}$) while phase provides a measurement of lag between the current and voltage waveforms. Using Eqs. 1-6, values for complex resistivity, conductivity, and permittivity were then calculated. As shown in Fig. 9a, measurements were made across two electrode strings with a total of 6 pairs available. Thus results presented are a measurement of the horizontal, as opposed to vertical, dielectric properties of the sea ice. For each separate pair of electrode strings, measurements were made across many combinations of electrodes. In the following analysis however, measurements are selected to determine permittivity at a specific depth. For instance, results presented from 0.15 m were obtained

through injecting and removing current at 0.10 m and measuring potential difference between electrodes placed at 0.20 m. This combination was then reversed with current being injected and removed at 0.20 m and potential difference measured at 0.10 m. For one depth, this routine was repeated for each of the 6 pairs of electrode strings. Each value of permittivity at a given frequency, depth, and date therefore represents the mean, and related standard deviation, of upwards of 12 measurements.

To gather measurements, electrode strings were connected to a set of instruments designed to regulate the current and measurement of potential difference (Fig. 10). A LabView-based program controlled these instruments and produced values of impedance and phase. Measurements were gathered over 13 frequencies ranging logarithmically from 10 Hz to 95kHz. Current was typically set to 10mA. Collection takes around 2.5 hours for one pair of electrode strings with up to 3 pairs of electrode strings being run in succession. This latter option, taking up to 8 hours, allows for fewer trips to the site; however, problems that arose from low temperatures and other factors resulted in temporary interruption of measurements. To minimize interruptions due to instruments losing power or seizing up in low temperatures, all equipment was placed in a tent with a small heater, along with a tarp to protect from condensation.

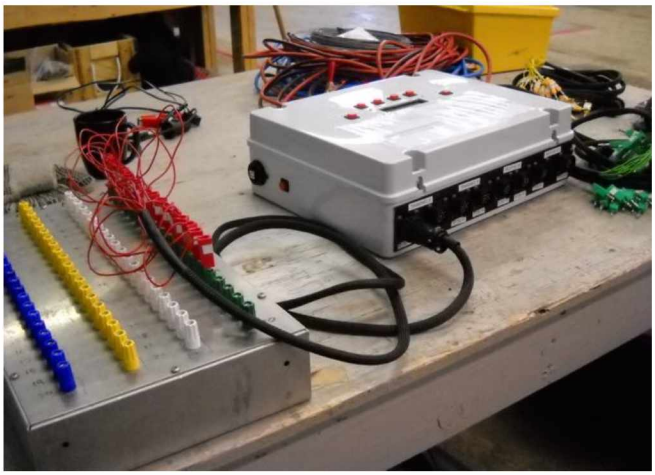

Fig. 10: Instrumentation used to obtain measurements of permittivity. Electrode strings are connected to the box on the left to control the location of current input and removal. It is powered by the control panel (on right) attached to a computer running a LabView-based program.

3.1.2 Pre-processing and Data Quality Assessment and Control

At each increment of depth examined in the following analysis (beginning at 0.15 m and increasing by 0.10 m), upwards of 12 measurements of impedance and phase were collected at each of the 13 frequencies. Resistivity, conductivity, and permittivity were calculated using Eqs. 1-5 for every individual measurement before calculating the mean and standard deviation between the several measurements. Before further analysis, measurements were reviewed to ensure their accuracy and identify any faulty measurements, which were then excluded from analysis.

A primary indicator of faulty measurements (blunders) to be excluded from further analysis was a positive measurement of phase. In a system where the current waveform leads the voltage waveform, a capacitor, phase will be negative. When phase was measured to be positive, the corresponding data point was therefore eliminated. The capacitance of sea ice and resultant phase is greatest at lower temperatures, when less brine and fewer pores are present in the system. For this reason, the number of data points removed tended to increase as the season progressed, the ice warmed, and phase decreased. Most of the removed points occurred at high frequencies, mainly 95 kHz.

A more widespread cause of measurements being excluded from analysis was a clearly identifiable and substantial impact by electrode polarization. This effect is less obvious when looking at individual datapoints and requires examination of weather conditions, ice properties, and comparison of complex permittivity measurements between months. Electrode polarization occurs when brine surrounds an electrode leading to the formation of an ionic double layer when a current is applied. This effect will cause a substantial increase in polarization, ε', particularly at the lowest frequencies. In parallel, ε'' will decrease due to the capacitive effect of the ionic double layer. While some effect has been measured when ice surrounds the electrode, the actual impact on measurements of permittivity is minimal. In lab-based studies, measurements of permittivity taken on brine of a given salinity can be used to determine the magnitude of the electrode polarization and assist in correcting measurements of complex permittivity of sea ice. Such an approach cannot be taken in the field where brine salinity is approximated and varies greatly throughout the depth of ice and with the seasons.

Small amounts of brine likely made contact with electrodes in all measurements throughout the year making it a challenge to determine when the amount of electrode

polarization present impacted measurements to a degree they needed to be removed. In 2013, electrode polarization was likely present but minor with no exclusion of data required. In 2014 however, electrode polarization did appear to impact measurements particularly those obtained in the upper 0.35 m of ice in May and all measurements from June. As a result, these measurements are excluded from the following analysis. Further description of the factors influencing this removal of data are presented in the Discussion section.

3.2 Ice Property Measurements

For each field trip, several ice cores were taken in parallel to make impedance measurements in order to obtain values of ice temperature, bulk salinity, and brine volume fraction throughout the depth of the ice. Cores were drilled within 2 m of the permittivity array and supplemented by measurements of ice temperature gathered at the UAF mass balance site. At least one core was gathered specifically for both temperature and salinity data. Temperature measurements were made using a Traceable © VWR Digital Thermometer immediately after core removal with readings taken at 0.05 m or 0.10 m increments down the length of the core. The impact of air temperature varied between field trips leading to the need to compare measurements to those gathered through the UAF Mass Balance station to assess the amount of error. As many core measurements did vary from these readings by upwards of 3 °C, the mass balance temperature measurements were determined to be of better use for the calculation of brine volume fraction. Salinity measurements were obtained by slicing ice into 5 cm thick sections, which were then bagged and brought back to the lab for melting. Subsequently salinity was measured using a YSI Model 30 © handheld salinity, conductivity, and temperature meter. Total estimated error for this meter is estimated to be no greater than +/- 2 %, with actual error being substantially less when calibrated and handled correctly.

3.3 Microstructural Analysis

3.3.1 Collection and Processing of Ice Samples

During each sampling campaign, cores for ice microstructural analysis were also obtained. Once removed, the ice was examined to identify 0.06 m sections representative of different ice textures and pore microstructures. Typically at least one sample was obtained in the top 0.20 m where granular ice is most likely present, a second at around 0.30-0.40 m depth where granular ice

transitions to columnar ice, and a third at greater depth where columnar ice is well developed. All samples were weighed and matched with a second sample of equal mass. The samples were next brought promptly back to the lab in an insulated container where they were centrifuged to remove all brine from open pores and channels. Each sample was then wrapped with aluminum foil and stored at -40 °C to preserve pore microstructure for further analysis after transfer in Dewar vessels to the Geophysical Institute Sea Ice Laboratory.

For x-ray computed tomography (CT) imaging, sample cylinders 50 mm in length and 30 mm in diameter were produced using a bandsaw and lathe at temperatures between -10 and 15°C. A Skyscan 1074 portable micro-CT scanner was used for x-ray tomographic imaging at –20°C. The scanner was initially calibrated to ensure the x-ray tube is performing well, the stage where the sample is place is centered, and to gather a flat field image for the given voltage, current, and exposure. This latter step helps to correct for irregularities in the camera and x-ray source. After calibration, several projection images were taken of the sample to determine the best setting for exposure time and if geometric correction and filtering needed to be applied. Individual vertical projection images were next gathered at 0.90° increments over ~180° totaling 201 projections for each sample. These images of a 16-bit TIFF format with pixel size of 40 μm x 40 μm were next reconstructed using NRecon software (Bruker microCT, Kontich, Belgium). Gray values are based on the attenuation of x-rays through the sample also referred to as radiodensity. For the samples of sea ice imaged, the spread of radiodensities and hence gray values (also known as CT numbers) extended from 0 to 1600. The former is associated with air. Through examination of several images, ice was found to have a mode centered around a gray value of 650 while brine, with no strong mode apparent in the majority of images, was responsible for the tail extending to higher values. Therefore when converting the projection images to a 3D volumetric stack of 8-bit JPEG images, bounds were set to include only pixels with gray values in this range. When values existed outside of this range, they were considered an artifact and excluded. This was only necessary for the first several samples processed due to the use of putty (of an unexpected high radiodensity) to hold the sample in place. In subsequent sampling, the putty was removed.

3.3.2 Processing of Images

To extract quantitative data on the microstructure of each ice sample, the tomographic data were further processed and analyzed. An average filter 3x3x3 voxels in size was first used to smooth the image (Fig.11).

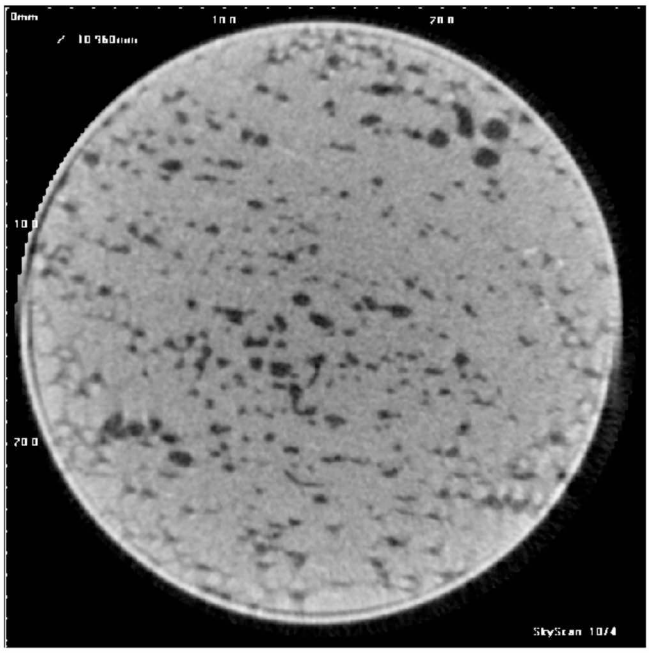

Fig. 11: Smoothed image from ice sample taken in June 2013 at a depth of 0.84-0.90 m. Note artifacts and gradient in shading present along the edge of sample, removed once ROI is applied.

To determine the location of the threshold delineating between ice and air, ranges of gray values were next determined through the selection of several regions representative of each. Gaussian curves were next fit to the distribution of values and the mode found for both ice and brine. The threshold was set to the value at which the two tails from the distributions overlap (Fig.12).

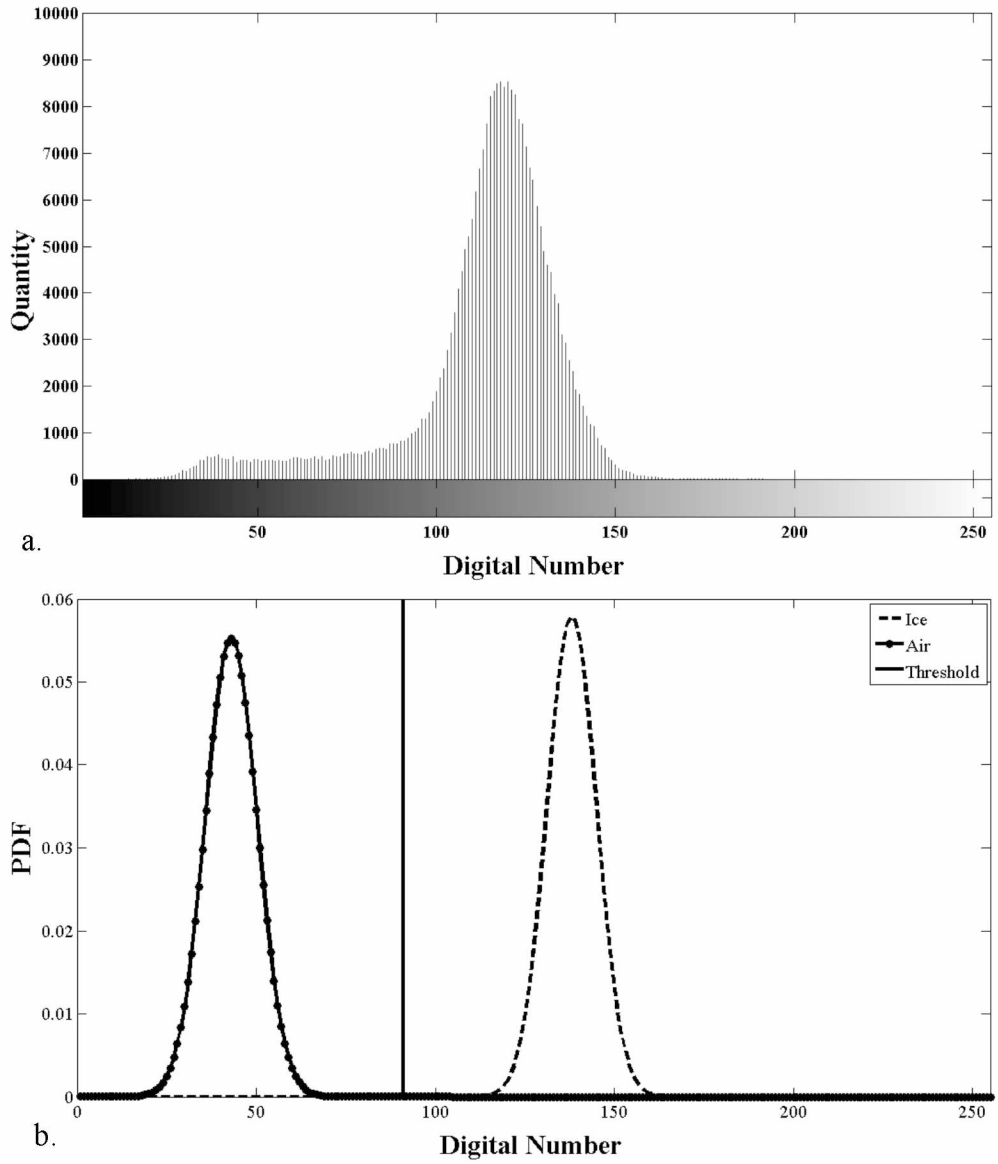

Fig. 12: a) Histogram of smoothed horizontal slice of 3D image taken of sample from June 2013 at a depth of 0.90-0.96 m; b) Results of maximum likelihood classification showing spread of values for ice and air. Threshold set at DN = 91.

Determining the threshold delineating between ice and brine presented a greater challenge. Due to variations in salinity, brine displays inconsistent radiodensity resulting in a wide range of gray values. In addition, regions of brine are much smaller than those for air and ice leading to a smaller sample size of values and a less apparent mode. Through manually identifying pixels of known brine in combination with examination of the original histogram, an approximate threshold was determined and applied across all samples. As only a small amount of brine was typically present, primarily in samples gathered at the coldest periods, this

approximation was found to be adequate. Once thresholds were determined, the image was binarized through setting all pores of either air or brine to 1, and ice to 0 (Fig.13).

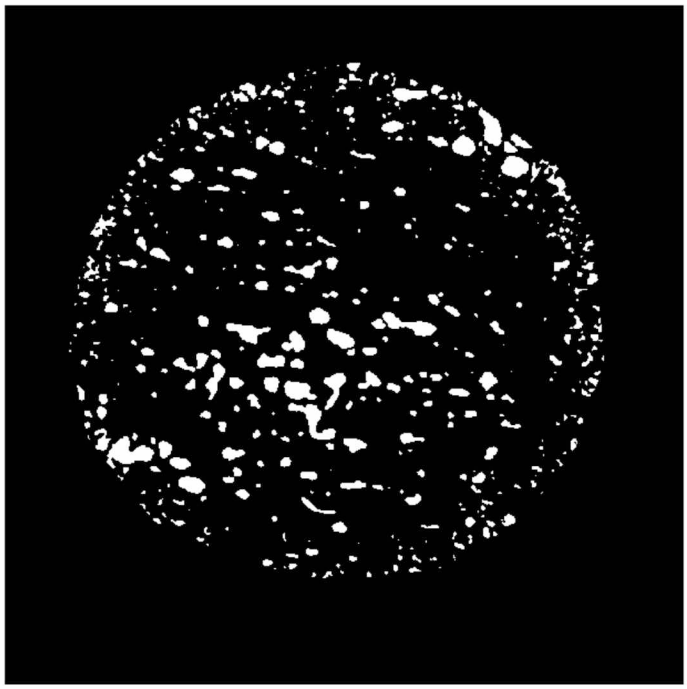

Fig. 13: Image after ROI applied, segmentation, and resultant binarization. Pores are in white, ice in black.

For the purpose of this study, it was imperative to obtain quantitative descriptions of individual pore spaces. Processing was done in MatLab using functions available in the Image Processing Toolbox. For each stack of images, pores were defined as clusters of 26-connected voxels (voxels sharing a face, edge, or corner) (see Fig. 14). The number of voxels and their placement were next recorded for each individual pore. This resulted in a large amount of data available to examine variations in pore geometry and extent.

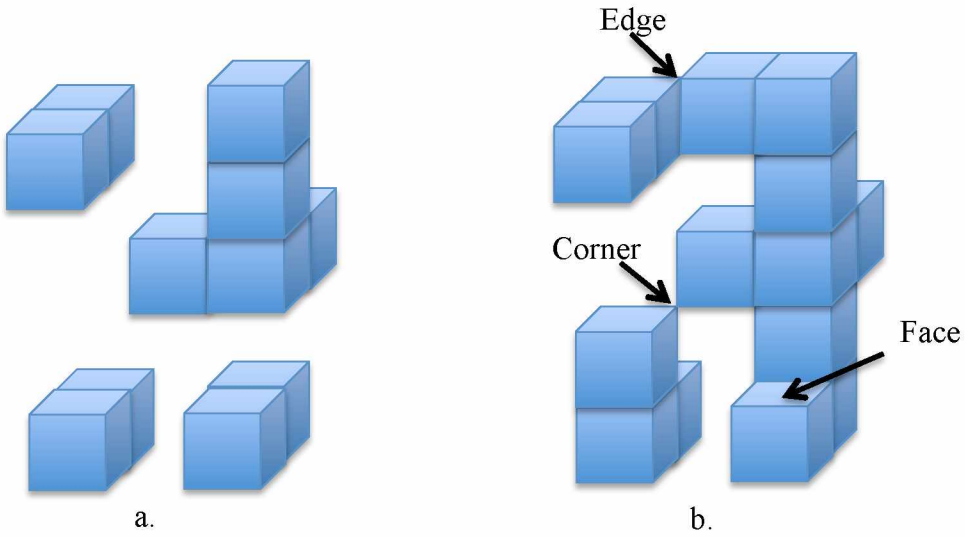

Fig. 14: a) Example of microstructure in voxel space. Shown are 4 separate pores with no connectivity present from the top to bottom; b) Pores in (a) evolved to become one pore connected from top to bottom assuming 26-connected neighborhood.

Pore volume and surface area were both initially determined for each individual pore. The former was found through summation of the number of voxels included while the latter required a coding routine found in Appendix A. In addition, the connectivity and horizontal extent of pores was examined. In past studies conducted by Pringle et al. (2009), a measurement of fractional connectivity was used to define the overall extent of pore networks. This characteristic is defined as the percentage of pores present at a given depth connected through any path to the uppermost layer. For each layer of the 3D stack of images, the pores present were identified and their topmost bound determined. The fraction of pores connected to the top layer decreased with increasing depth in the sample, in most cases to zero.

Chapter 4: Results

4.1 Error Analysis

4.1.1 Measurements of Complex Permittivity

Measurements gathered in the upper 0.35 m of ice in May 2014 and all those made in June 2014 are not included in the discussion of results due to the impact of electrode polarization. This exclusion was determined through both examination of individual measurements and consideration of weather conditions. As noted above, electrode polarization leads to formation of a capacitive layer at the electrode/brine boundary, lowering values of ε''. In 2013, electrode polarization was likely present but minor with no exclusion of data required. This finding is illustrated by measurements of ε'' which show a gradual increase from March through June in parallel with an increase in temperature and brine volume fraction. In 2014, however, electrode polarization appears to have impacted measurements with ε'' showing a decrease between May and June, particularly in the upper layers of ice. Given an increase in temperature and brine volume fraction, connectivity and hence dielectric loss measurements are expected to increase which would increase ε''. We therefore postulate that capacitive effects outweighed the signal associated with sea ice permittivity itself. In early May 2014, snow depth dropped sharply by nearly 0.10 m over a 3-day period of above freezing temperatures. Salinity decreased in the upper layers of the ice during this time, suggesting the drainage of high-density brine and meltwater downward through newly connected pore space. Such movement is likely to increase the amount of brine surrounding electrodes in the upper layers of the ice leading to an increase in electrode polarization. In addition, with a decrease in snow depth solar heating of electrodes in the upper layers will further contribute to brine layer formation.

At each depth and frequency, upwards of 12 measurements were gathered over a time period of up to two days. In addition to electrode polarization, physically non-sensical measurements were excluded. This was most common in measurements made when the ice had a temperature above -2 °C, and at frequencies above 50 kHz. These factors often led to only 8-10 measurements being processed for further analysis. The standard deviation of these remaining measurements is likely a reflection of heterogeneities in ice temperature, salinity, and structure between pairs of electrode strings. In March, when temperatures were at their coldest, standard deviation was minimal likely due to smaller brine volume fraction and related horizontal variability in temperature and salinity. As the ice warms, brine channels and layers will widen

leading to an increase in both microstructural and electrical vertical anisotropy (Ingham et al., 2008). Given the persistent under-ice ocean currents at the measurement location, lamellae will be strongly aligned, resulting in microstructural horizontal anisotropy as well. When measurements of DC conductivity and permittivity are examined in relationship to their orientation to lamellae, sensitivity to this horizontal anisotropy is evident but challenging to quantify. The increase in standard deviation observed particularly in measurements of ε' and ε'' gathered in June is therefore attributed partially to an increase in vertical and horizontal anisotropy.

4.1.2 Ice Properties

As mentioned previously, due to bias in temperature data obtained for ice cores exposed to the air, *in situ* ice temperature measurements gathered at the UAF mass balance site were used in calculation of brine volume fraction and subsequent analysis in an effort to reduce errors. Such measurements were obtained using a string of thermistors frozen vertically into the ice. Each thermistor, placed at 0.1 m depth increments, houses a metal bridge across which resistance (derived from voltage) is measured every 15 minutes and recorded by a data logger placed above the ice. Measurements are next converted to temperature using the Steinhart-Hart equation. Two control bridges to compare voltage measurements are located in the data logger with the bridge used alternating between each thermistor. While thermistors are initially accurate to within +/- 0.1 °C, a small amount of error can be introduced with the transfer of measurements to the data logger and uncertainty associated with the Steinhart-Hart equation. Furthermore, comparison to the two control bridges causes variation between even thermistors (0.20 m, 0.40 m, 0.60 m, etc.) and odd thermistors (0.10 m, 0.30 m, 0.50 m, etc..) resulting in the zig-zag pattern seen in Fig. 16. To quantify this error, temperature measurements taken below the ice in isothermal ocean water were compared to those measured by a CTD (accuracy of +/- 0.02 °C) located within 5 m of the thermistor string. On average, even thermistors measured 0.057 °C above the CTD temperature while odd thermistors, 0.099 °C below the temperature. Overall, this error does not affect results significantly.

Assessing error in salinity measurements is more challenging as core removal is the most dependable and often only method available in the field. The salinity values used for calculation of brine volume fraction and analysis were the average of measurements gathered on 1 to 3 cores. Variations in S can be caused by actual differences in ice conditions. In addition, with the

removal of cores, brine will immediately drain from the ice (in particular the bottom-most core segment) thus lowering values of S. Standard deviation of bulk salinity for upwards of 3 cores obtained during each field visit was less than 1 ppt below a depth of 0.10 m. Above 0.10 m, the magnitude of standard deviation increased in March of 2013 and 2014 to a maximum of 3 ppt. Assuming the relationships presented by Cox and Weeks (1983) and Leppäranta and Manninen (1988) a 1 ppt difference in salinity can result in upwards of a +/- 2 % variation in brine volume fraction percentage when temperatures are below – 2 °C. When temperatures are greater than – 2 °C, the impact on brine volume fraction will vary depending on the temperature and average salinity, with upwards of a 10 % difference in brine volume fraction.

4.1.3 Image Processing

The dimensions of each horizontal slice of the volumetric CT image stack used in microstructural analysis are 736 x 736 x 1 voxels with one voxel being 40 x 40 x 40 μm^3 in volume. Assuming air has a digital number of 45 and ice has a digital number of 147 (see Fig. 12), at least 53% of the voxel, equal to 32 μm^3, must be filled with air for the voxel to have a digital number below the air-ice threshold placed at a digital number of 91. As contrast between these two phases decreases, the minimum volume of a detectable feature will increase and vice-versa. As no mode for brine was able to be determined, a minimum feature size is harder to define. Assuming an ice-brine threshold set at a digital number of 160 however, the minimum feature volume necessary to be detected ranges from 20 μm^3 to 37 μm^3 depending on the contrast between the ice and brine. While pore throats and crystal boundaries may at times be smaller in size than these minimum-detectable volumes, brine pores and channels are often orders of magnitude larger (see Table 1). Therefore, for the purpose of this study focused largely on bulk properties and trends in microstructural evolution, these sources of error were not further addressed.

The thresholds set to delineate ice, brine, and air may also affect measurements of microstructural characteristics. A threshold to discriminate between air and ice was derived through maximum likelihood classification. However, the approach taken to distinguish between brine and ice was less precise. No large pore cross-sections with brine were present, the result of centrifuging ice samples. A final threshold was determined through examining images with known brine-filled pores and varying the placement of the threshold until an accurate representation of these pores was obtained. The result was next applied to other images to

determine its accuracy and dependability. This method could be improved by measuring the attenuation coefficient of brine at varying salinities. As brine salinity may vary between pore spaces, approximations of attenuation in relationship to ice temperature and brine volume fraction would also be useful. Due to the small amount of brine present in the system, this latter method was not pursued.

4.2 Comparison of 2013 and 2014 Ice Growth Conditions

4.2.1 Weather Conditions and Seasonal Cycle of Ice Growth and Melt

Air temperature, snow depth, and ice thickness between January, when the mass balance site and electrode strings were emplaced, and June, when all instruments were removed are presented in Fig. 15. Up until the first week of April, conditions were relatively similar between 2013 and 2014 with air temperatures ranging between -10 °C and -35 °C. During this time ice thickened at a constant rate, with ice formed in 2014 growing slightly faster than that formed in 2013. Starting in mid-April, air temperatures measured in 2013 and 2014 began to deviate significantly.

Except for a brief period in mid-May, air temperatures remained below freezing in 2013 until May 21st. After this time, ice growth stagnated along with a decrease in snow depth. Ice thickness began to decrease on June 2nd. In 2014 however, air temperatures showed their first abrupt rise to only a few degrees below freezing on April 13th. The first persistent above freezing temperatures occurred on May 1st accompanied by substantial snowfall and eventual snow melt as temperatures remained above freezing for 2-3 days. During this warming event ice thickness began to decrease, a full month earlier than in 2013. After May 21st, mass balance instruments stopped taking measurements due to technical problems until final data were collected on their removal on June 8th. During this time, ice thickness was not observed to decrease substantially with a drop in air temperature to below freezing between May 21st and June 8th, 2014. Given the variation in weather conditions, ice growth and the resultant microstructure of the ice likely differed substantially.

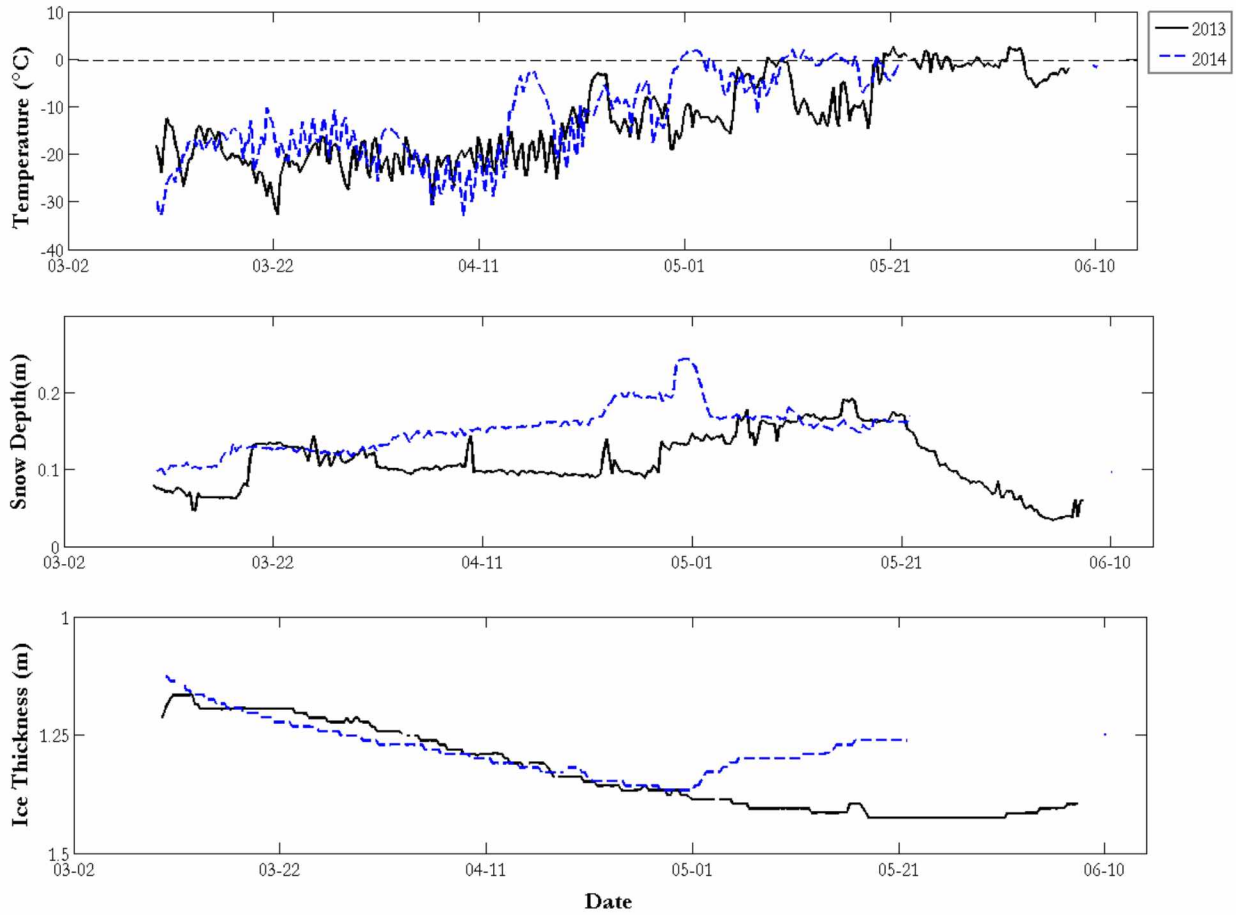

Fig. 15: Time series of air temperatures, snow depth, and ice thickness. Data from 2013 and 2014 are shown.

4.2.2 Ice Properties

Measurements of ice temperature, bulk salinity, and calculated brine volume fraction as a function of depth are shown in Fig. 16. Contrasting weather conditions in 2013 and 2014 are reflected in differences in ice properties, beginning with differences in ice temperature profiles in March. In 2013, ice temperatures in the upper 1.0m are nearly 4 K lower than in 2014. The bottom 0.30-0.40 m of ice were also found to vary substantially with 2014 ice having temperatures slightly below freezing in comparison to 2013 when ice temperature increased gradually throughout the depth of ice. Despite differences in ice temperature, bulk salinities were similar between the two years, ranging between 4 and 6 ppt. Brine volume fractions reflect contrasting ice temperatures, with values in 2014 higher than in 2013 particularly in the 0-1.0 m depth interval.

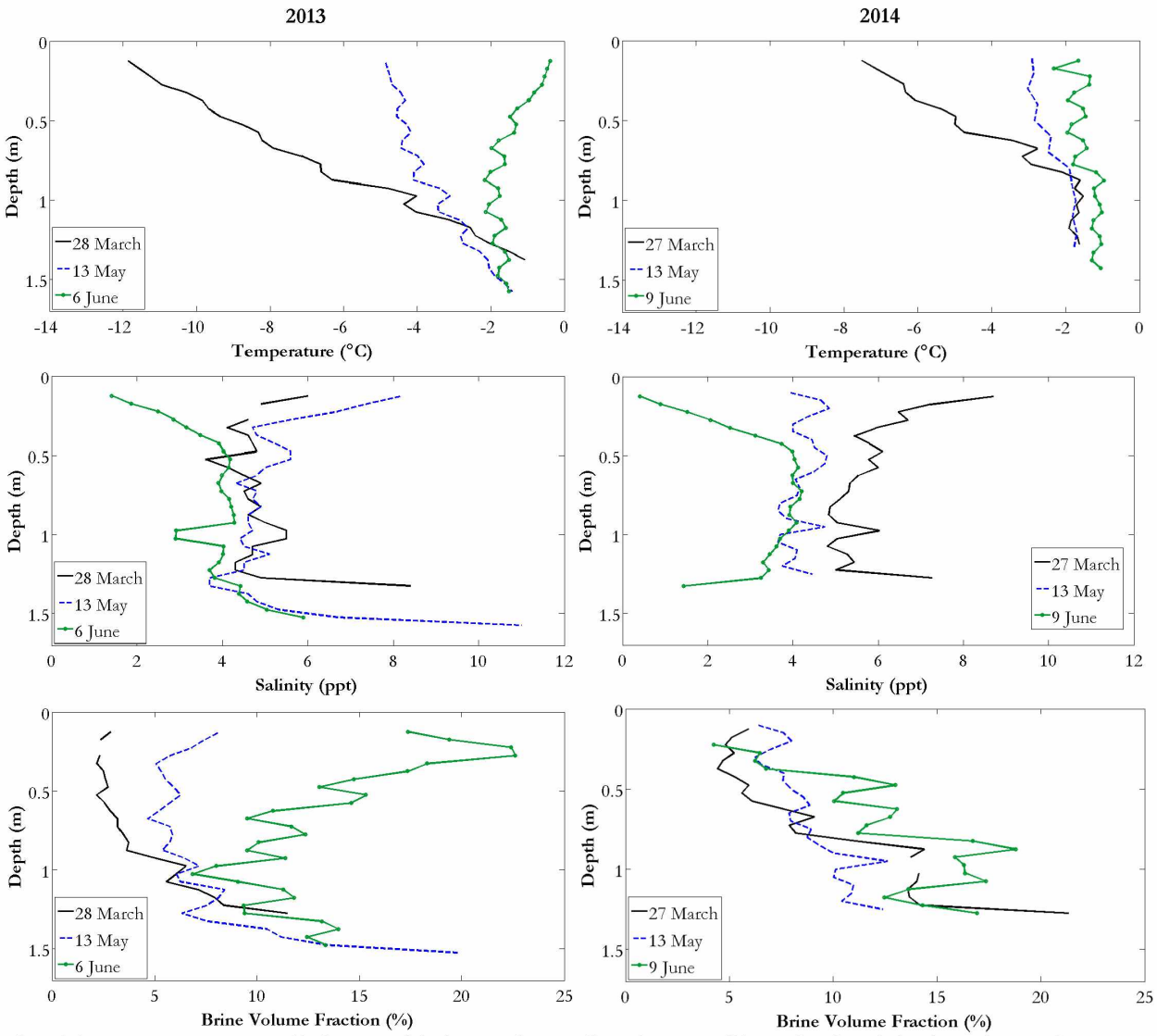

Fig. 16: Temperature, salinity, and brine volume fraction profiles obtained during the spring season of 2013 and 2014. Temperature measurements were obtained from the UAF mass balance site located within 10 m of the permittivity array and are uncorrected for the small source of error explained in Chapter 4.1.2 . Salinity measurements were obtained from ice cores also adjacent to permittivity array. Brine volume fraction was calculated using the empirical formulas presented by Cox and Weeks (1983) and *Leppäranta, and Manninen* (1988).

May core measurements mirror the strong contrast in weather conditions recorded between 2013 and 2014. In 2013, ice temperatures remained lowest at the top of the ice linearly increasing to the freezing point of seawater at the ice/ocean interface. Bulk salinity increased in the upper and lower layers in May while maintaining values relatively equal to those measured in March between 0.50-1.10 m. Brine volume fraction increased in the upper 1.0 m to values just above 5%. In 2014, little variation in temperature was found throughout the ice with the upper

1.0 m being no more than 1 °C less than values measured at the bottom of the ice. A substantial decrease in salinity was concurrently measured throughout the ice. The upper 0.50 m in particular displayed a sharp drop in values resulting in a salinity profile with near-constant values around 4 ppt throughout. Brine volume fraction was found to increase in the upper 1.0 m before holding constant towards the bottom of the ice.

In June, ice property measurements from 2013 and 2014 display similar behavior. Ice temperature in 2013 is shown to surpass those measured in 2014 in the upper 0.50 m. At greater depths however, temperatures remained higher in 2014 than in 2013. Salinities in both years were measured to be relatively equal showing a linear increase from just above 0 ppt to 4 ppt in the upper 0.50 m. Resultantly, very high values of brine volume fraction were calculated for the upper 0.50 m of 2013 ice, with values decreasing with depth. The inverse behavior was observed in 2014 with values of brine volume fraction being at a minimum in the upper layers, increasing to the bottom of the ice.

4.3 Measurements of Low Frequency Complex Permittivity

Measurements of ε' and ε'' were initially examined in terms of frequency. Differences between measurements at varying depths and between the two years were apparent, surmised to be related to variations in ice properties, texture, and microstructure.

4.3.1 The Real Part of Complex Permittivity vs. Frequency

In 2013 and 2014, an increase in ε' is seen as the season progresses. The magnitude of this increase varies with depth (Fig. 17). Below 1000 Hz measurements show the greatest increase between March and June. In 2013, the increase in ε' is greatest in the upper layers, above 0.45 m, where ice is most sensitive to variations in weather conditions and ice textural transitions from granular to columnar. At 0.75 m, the increase between March and May remained relatively equal to layers above however the increase from May to June lessened. At 1.05 m little variation is seen throughout the season. Measurements of ε' gathered in 2014 were substantially higher than those gathered in 2013 by upwards of an order of magnitude. Similar trends persisted however with the greatest increase found between March and May at depths down to 0.75 m. At 1.05m, the proximity to the ice-ocean interface kept the ice at the freezing point and resulted in comparatively small differences between years.

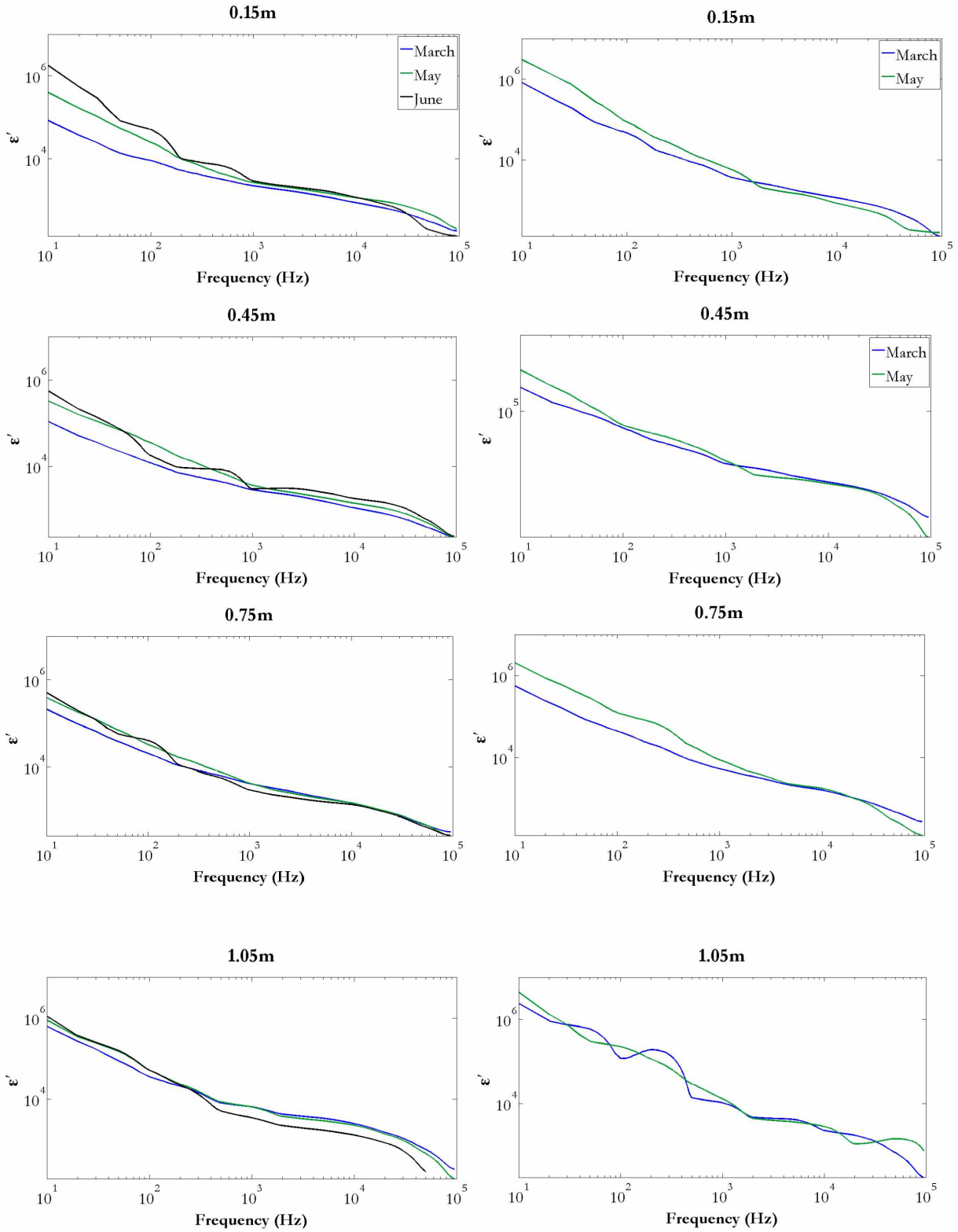

Fig. 17: Measurements of the real part of the complex permittivity (ε') as function of frequency for March through June of 2013 and March of 2014.

4.3.2 The Imaginary Part of Complex Permittivity vs. Frequency

Fig. 18 shows measurements of ε'' in relationship to frequency. A clear increase is seen across all frequencies between March and June in 2013 and March and May in 2014. In 2013, the upper layers show a greater increase in comparison to lower layers. This result alludes to variations in ice properties and texture associated with the transition from granular to columnar ice. Examining measurements from 2014, differences between measurements made on upper and lower layers are less defined given the lack of data from June. Similar to measurements of ε', values of ε'' in March were substantially higher than those gathered the previous year.

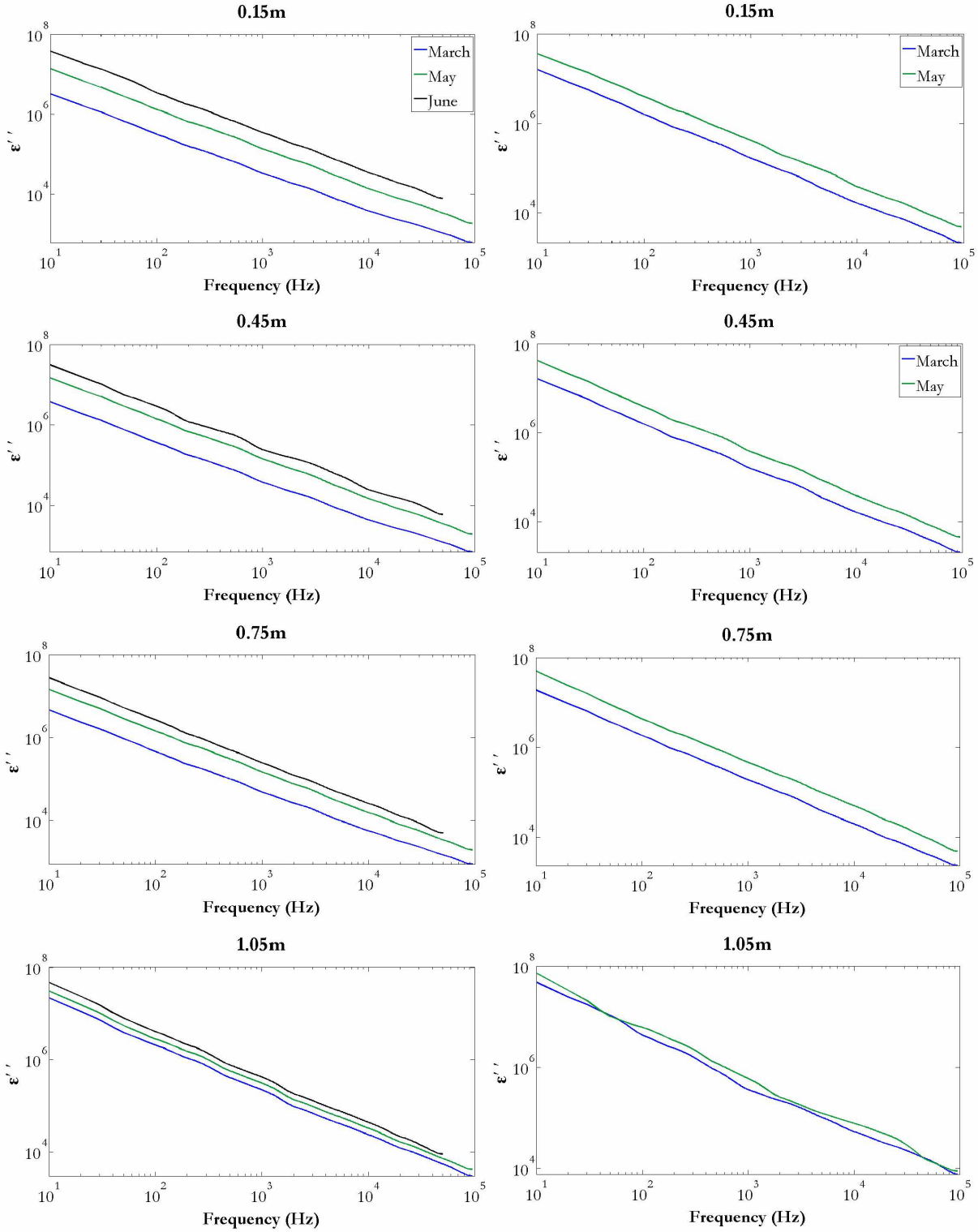

Fig. 18: Measurements of the imaginary part of the complex permittivity (ε'') as a function of frequency for measurements gathered in March through June of 2013 and March and May of 2014.

4.4 Ice stratigraphy and x-ray tomography of pore microstructure

Vertical thick sections were cut from 2013 and 2014 cores to determine the depths at which ice of granular texture begins to transition to that of columnar. Results are presented in Fig. 19. In 2013, the upper 0.2 m were composed of frazil crystals creating a layer of granular ice. Over the next 0.1 m ice crystals are shown to transition evolving to be larger in size and elongated in the vertical. By 0.3 m this texture characteristic of columnar ice is well established, continuing to the bottom of the ice core. Samples gathered in 2014 show a slightly thicker layer of granular ice, extending several centimeters past 0.2 m depth. This is followed by a shorter transition before columnar ice is, again, clearly established by 0.3 m depth.

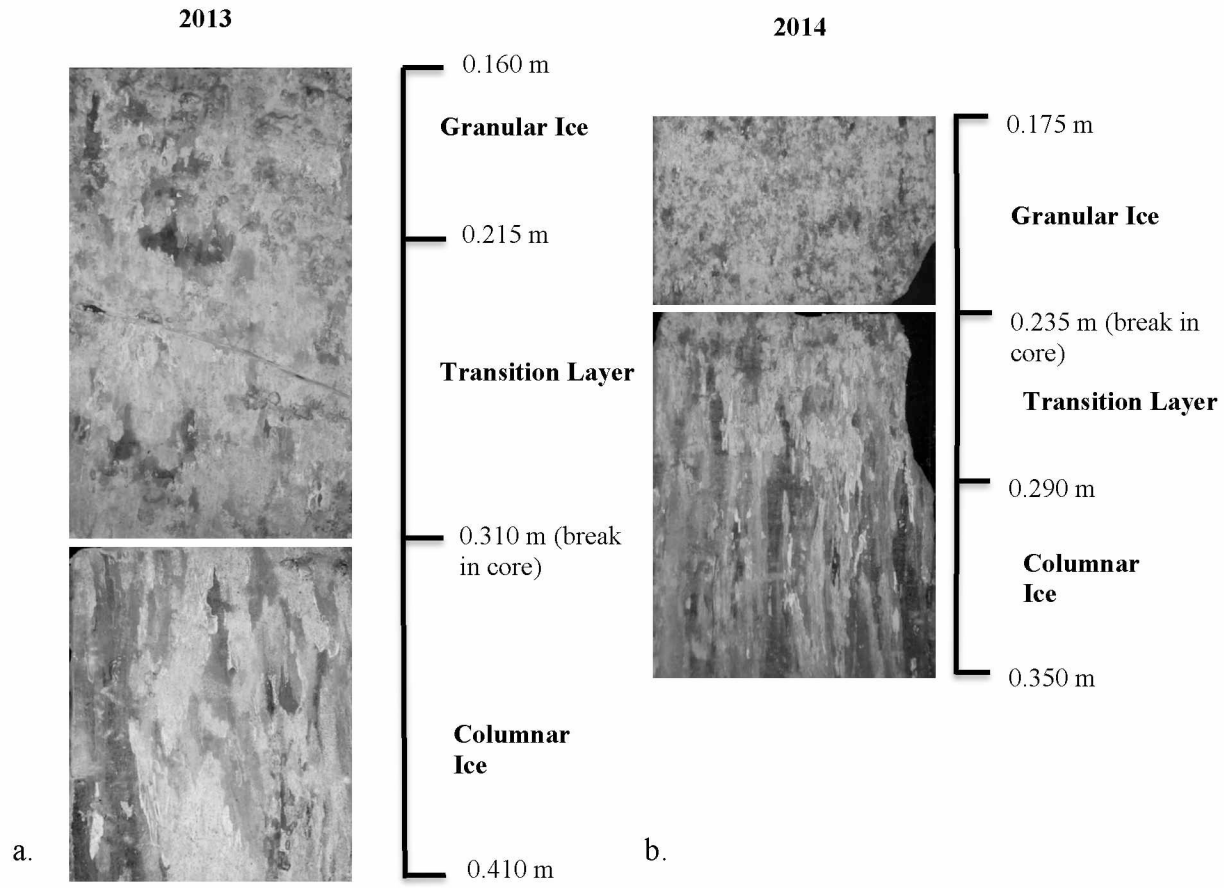

Fig. 19: Variations in ice microstructure with depth. Vertical thin sections from 2013 (a) and 2014 (b) showing variations in crystal orientation with depth.

Ice texture will determine the size, distribution, and geometry of brine pores. Fig. 20 shows 3D images gathered in the upper granular and transition layer and at greater depth where columnar ice is well established. In March, upper layers display a highly disconnected pore

space. At greater depth where columnar ice is established, number density of pores is higher, with brine inclusions often connected vertically and aligned with the ice lamellae. Samples gathered in June show a clear evolution. In the granular layer, large pores are present extending in the vertical and horizontal directions. Columnar ice is composed of pores also having enhanced connectivity but primarily in the vertical direction with any horizontal growth in pore size occurring parallel to ice lamellae. While seasonal evolution of ice microstructure is understood and clearly evident when examining such 3D images, to determine the relationship between measurements of complex permittivity and this microstructure, further analysis must be conducted to quantify pore space characteristics. In the following, the distribution of pore volumes, the overall geometry of the pore space (defined by surface area to volume ratio), and pore connectivity are determined for samples gathered from March through June of 2013 and 2014.

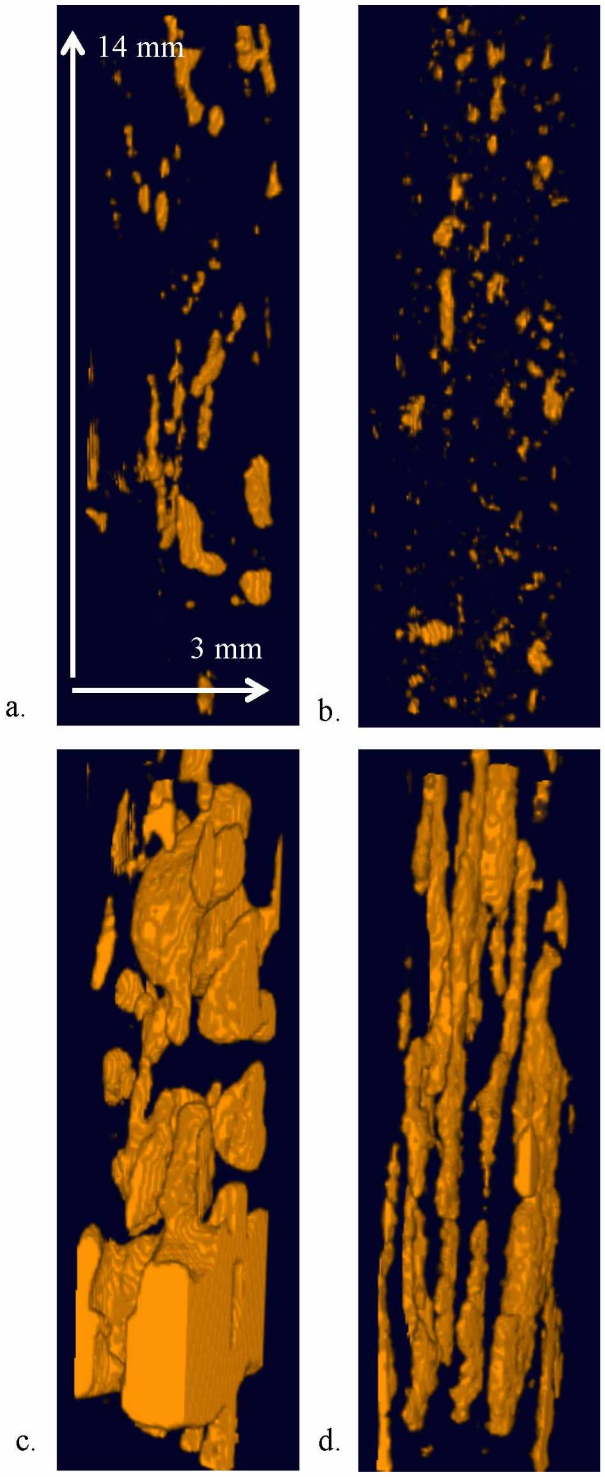

Fig. 20: 3D images derived using x-ray CT techniques. a) March 2013: 0.20-0.26 m, b) March 2013: 0.88-0.94 m, c) June 2013: 0.20-0.26 m, d) June 2013: 0.90-0.96 m.

4.4.1 *Pore Volume Distribution*

Brine volume fraction (BVF), derived from measurements of ice temperature and salinity, is often used to provide an estimation of pore connectivity and a general description of microstructure. It remains unknown, however, how individual pore volumes may vary within ice of similar BVF. For example, 10% BVF could be the result of only 2 pores holding 5% BVF each, 10 pores holding 1% BVF each, or any other combination of pore volumes. This difference in distribution of brine within the ice matrix may result in variances in ε' and ε''. Fig. 21 presents the portion of total brine volume fraction created by pores of various sizes. Comparison of BVF of samples and from cores are presented in Table 3 with curves presented in Fig. 21 being derived using the former.

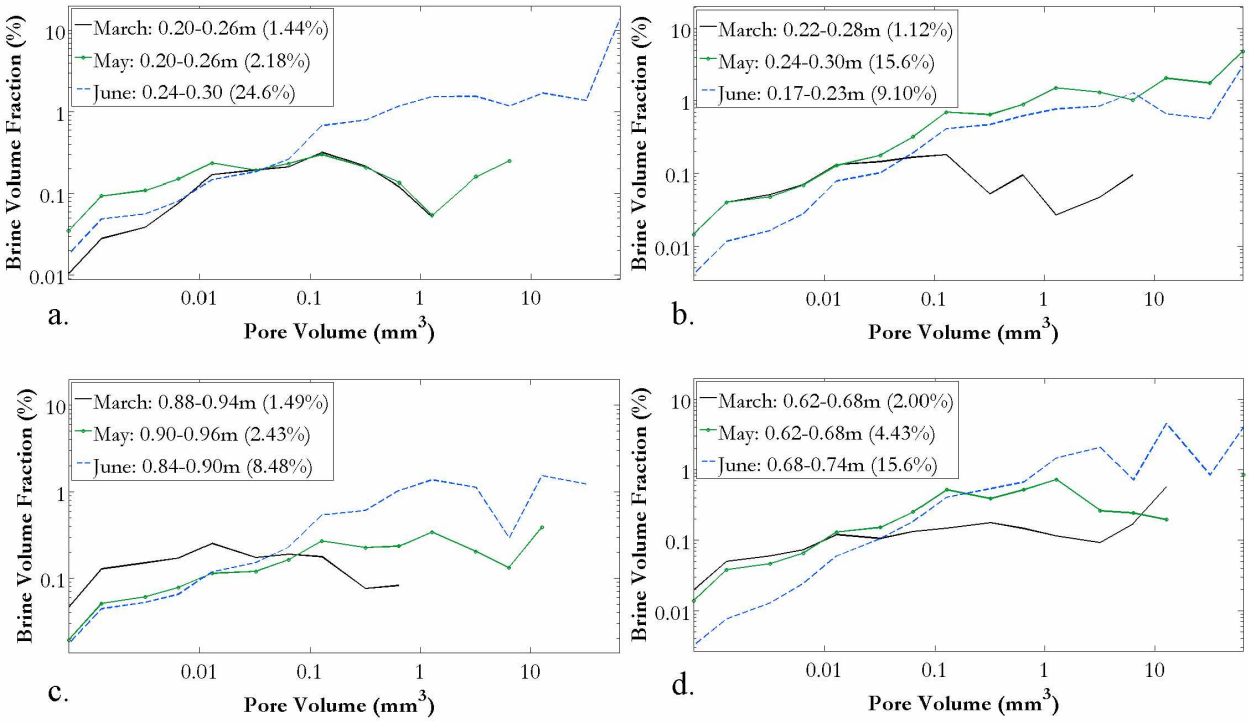

Fig. 21: Evolution of pore volume distribution derived from ice samples gathered in 2013 (a and c) and 2014 (b and d).

Table 3: Comparison of bulk brine volume fraction calculated using core measurements of temperature and salinity to brine volume fraction of microstructural samples.

Date/ Depth	BVF of Core (%)	BVF of Microstructural Sample (%)
March 2013: 0.20-0.26m	2.3	1.44
March 2013: 0.88-0.94m	4.3	1.49
May 2013: 0.20-0.26m	6.8	2.18
May 2013: 0.90-0.96m	6.4	2.43
June 2013: 0.24-0.30m	22.6	24.6
June 2013: 0.84-0.90	9.5	8.48
March 2014: 0.22-0.28m	4.7	1.12
March 2014: 0.62-0.68m	8.5	2.00
May 2014: 0.24-0.30m	6.5	15.58
May 2014: 0.62-0.68m	8.3	4.43
June 2014: 0.17-0.23m	4.3	9.10
June 2014: 0.68-0.74m	11.6	15.55

In 2013, upper layers evolved slowly from March to May with the small 0.74% increase in total BVF primarily coming from an increase in pores $<0.1 mm^3$ in size. By June, BVF increased over 22% reaching the highest value out of all the samples. An increase in pores $> 0.1 mm^3$ is evident with the portion of total BVF contained in pores of lesser volume decreasing to below 0.01%. In the lower columnar layers, a different trend is present. The 0.94% increase in BVF between March and May comes from an increase in pores $> 1 mm^3$ while the amount of volume stored in smaller pores decreases. In June, the BVF held in pores $> 1 mm^3$ increases 5.3% while the percentage of volume in pores $< 0.1 mm^3$ remains constant.

Different weather conditions in 2014 led to substantially different evolution of pore distributions particularly in the upper layers. Fig. 21 reveals a large increase in BVF from March to May. This increase can be attributed to the addition of pores > 0.1 mm^3 holding near to 14.3% BVF in comparison to only 0.53% in March. A 6.5% drop in BVF occurred as ice evolved into June with the percentage decreasing relatively equally across all pore volumes. The lower, columnar layers displayed a gradual increase in BVF from March through June. The 2% rise between March and May can be attributed to an increase in pores > 0.01 mm^3. In June, a decrease in pores < 0.01 mm^3 is evident with an 11.5% rise in the BVF held in pores > 1 mm^3.

4.4.2 Surface Area to Volume Ratio of Pores

Surface area to volume (SA/V) ratio provides an overall approximation of pore smoothness with lower values representative of pore spaces having fewer roughness features. Results in Fig. 22 show a decrease in SA/V ratio (an increase in smoothness) as ice evolves from March through June in the upper granular layer. In 2013, both March and May data show a broad distribution of SA/V ratios with a relatively constant amount of brine volume fraction associated with pores of a SA/V ratio < 2. By June, lesser variability in SA/V ratio was found with 17% brine volume fraction having a SA/V ratio < 0.4. In the lower layers, SA/V ratio decreases between March and May with 1.5% of the BVF increase occurring in pores with a SA/V ratio <1. A further increase in the amount of pores of this SA/V ratio narrows the overall distribution as BVF grows 6% in June.

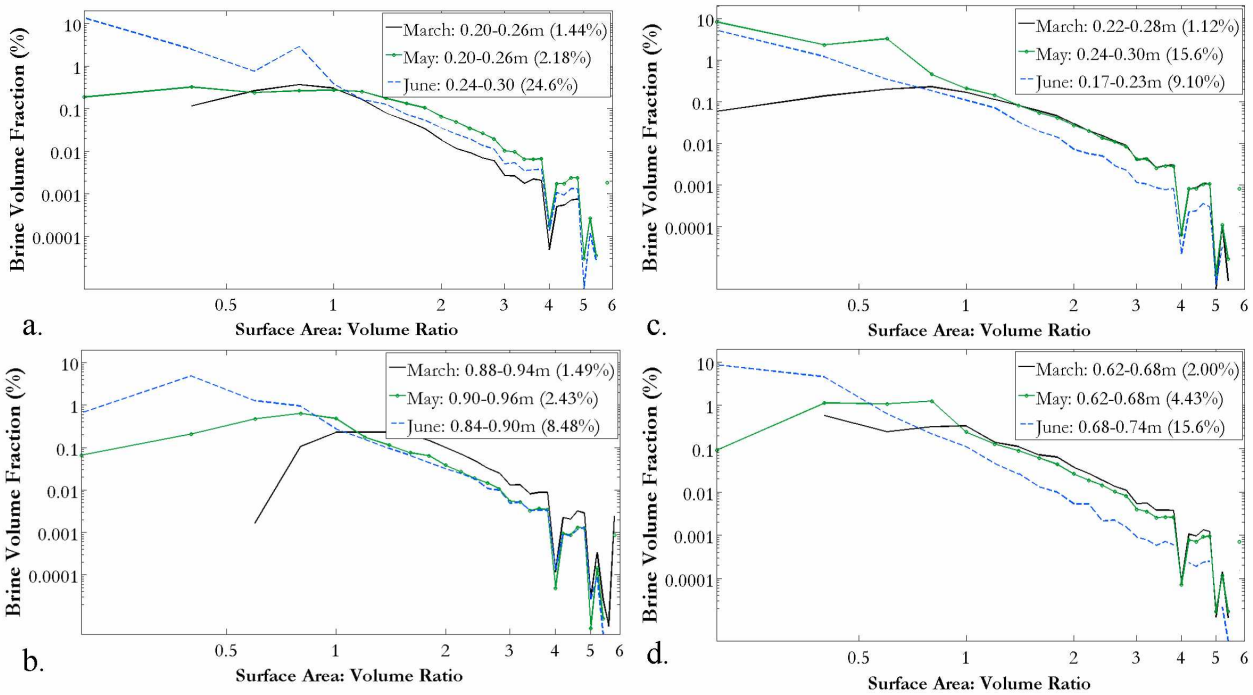

Fig. 22: Evolution of surface area to volume ratios derived from ice samples gathered in 2013 (a and c) and 2014 (b and d).

In 2014, the 14% increase in BVF from March to May in the upper layers of ice led to a greater portion of pores with SA/V ratios <1. In June, a 6% decrease in BVF is spread across all values of SA/V ratios thus maintaining the general distribution found in May. Examining the columnar layer, the SA/V ratio is shown to decrease from March through June with the percentage of BVF associated with values <1 gradually increasing to 13% while decreasing at values above >1. As a result the overall distribution in June again narrows from that seen in March and May.

4.4.3 Pore Connectivity

The measurement of fractional connectivity provides another method to track pore evolution from March through June independent of pore size and geometry and is of greatest use in evaluating ice permeability. In 2013, the fractional connectivity of the upper granular/transition layer is shown to hold constant between March and May with samples having only 25% connectivity by 1.0 mm from the top of the sample (Fig. 23). In June, the connectivity throughout the sample, while small, is still present with 1.2% of pores in the bottom-most layer connected to the top. In the lower columnar layer, a gradual increase is shown with the depth of

25% connectivity increasing from 0.5 mm to 1.2 mm and finally to 3.6 mm. By June, 1.5% of pores are still connected to the top layer.

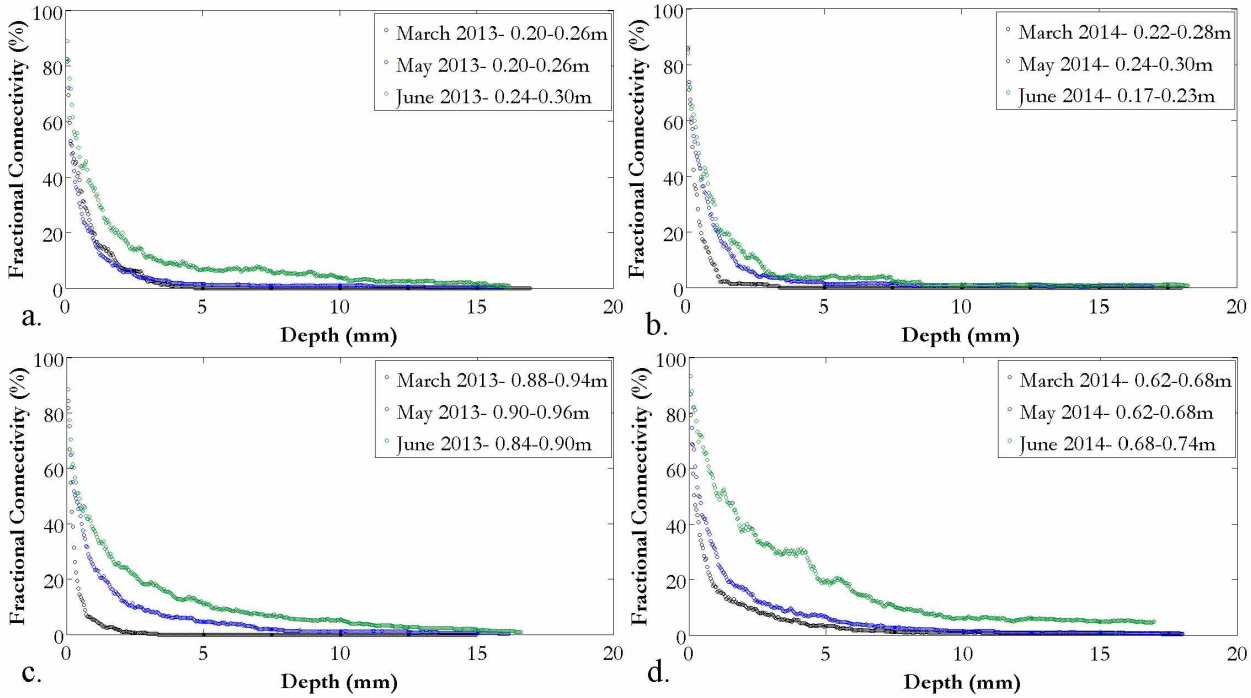

Fig. 23: Evolution of fractional connectivity derived from ice samples gathered in 2013 (a and c) and 2014 (b and d).

The large increase in BVF from March to May of 2014 cited above is not necessarily evident when examining fractional connectivity. During this time, the depth of 25 % connectivity increases only from 0.7 mm to 1.0 mm. In June, this value increases another 0.3 mm to 1.3 mm with the sample never showing through connectivity. The lower layers show a much different trend. The depth at which at least 25 % is present increases from 0.8 mm to 1.5 mm between. In June, this value increases to 5.6 mm depth with 5.2% connectivity between the bottom and top layer.

Chapter 5: Discussion

5.1 Examination of Complex Permittivity Measurements in Relationship to Ice Properties

5.1.1 The Real Part of the Complex Permittivity

The real part of the complex permittivity, ε', is a measure of a material's polarization and ability to store energy when a current is applied. Measurements of ε'' are compared to ice temperature in Fig. 24 with a summary of correlations found at frequencies below 10,000 Hz in Table 6.

Temperature and ε' were found to be most strongly correlated in 2013 at frequencies below 100 Hz. In 2014, correlation coefficients were somewhat lower but near-constant below 1000 Hz. Hence, the combined data show strongest significant correlation ($p < 0.05$) between ε' and ice temperature at frequencies below 100 Hz. Establishing causal relationships based on these findings presents challenges due to temperature having a contrasting effect on the individual electric properties of ice and brine. An increase in temperature in pure ice leads to the weakening of bonds along crystal boundaries and an increase in the concentration of defects resulting in an increase in ε' (Petrenko and Whitworth, 1999). Conversely, an increase in temperature will lead to a weakening of the natural structure of molecules in an ionic solution such as brine (H_2O, NaCl) thus lowering values of ε'. When all other factors are excluded, the positive correlation between temperature and ε' therefore indicates that the electric properties of ice dominate those of brine in measurements of ε' of sea ice. The negative relationship found between ε' and bulk salinity contradicts this result however (Fig. 25, Table 5).

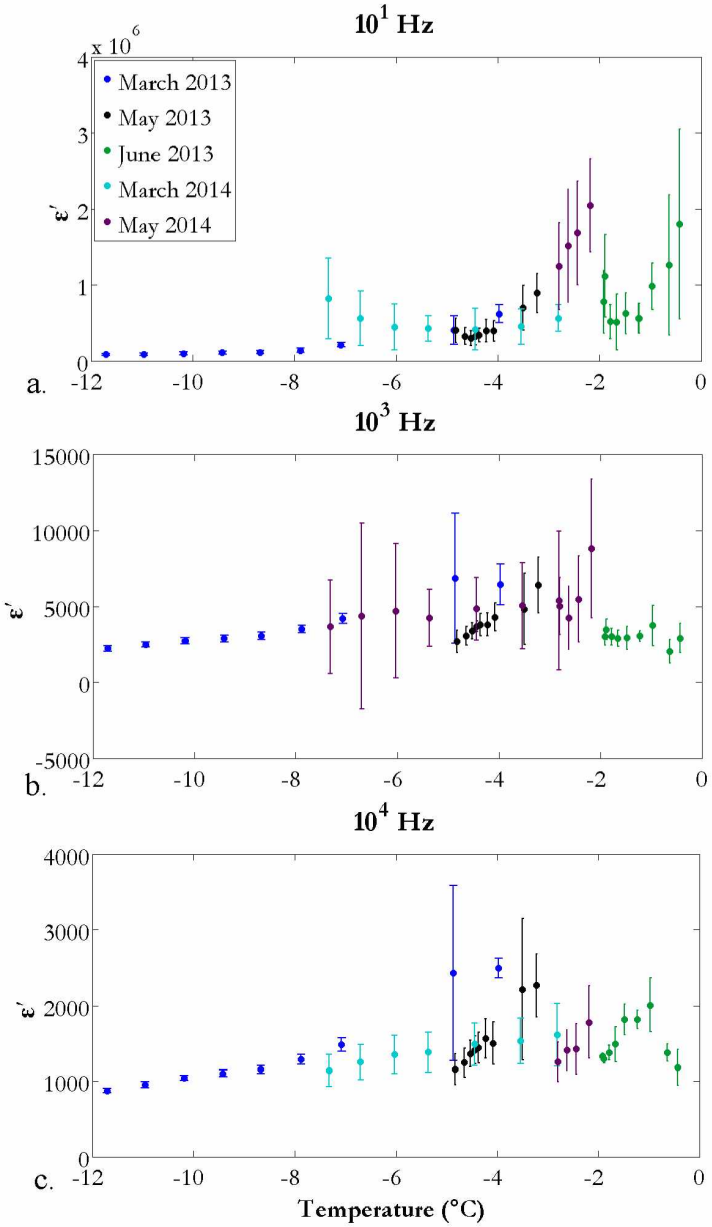

Fig. 24: Real part of the complex permittivity (ε') as a function of ice temperature for measurements gathered in 2013 and 2014 at depths between 0.15 m to 1.05 m and frequencies of a) 10^1 Hz, b) 10^3 Hz and c) 10^4 Hz. Bars denote plus/minus one standard deviation.

Table 4: Correlation coefficient between ε' and temperature for measurements gathered in 2013, 2014, and 2013 and 2014 combined.

	10 Hz	20 Hz	50 Hz	100 Hz	200 Hz	500 Hz	1000 Hz	2000 Hz	5000 Hz	10,000 Hz
2013	0.78	0.82	0.75	0.75	0.50	0.52	0.14	0.27	0.40	0.47
2014	0.56	0.54	0.59	0.51	0.57	0.60	0.62	0.12	0.19	0.20
2013 & 2014	0.51	0.48	0.48	0.48	0.36	0.39	0.26	0.25	0.35	0.39

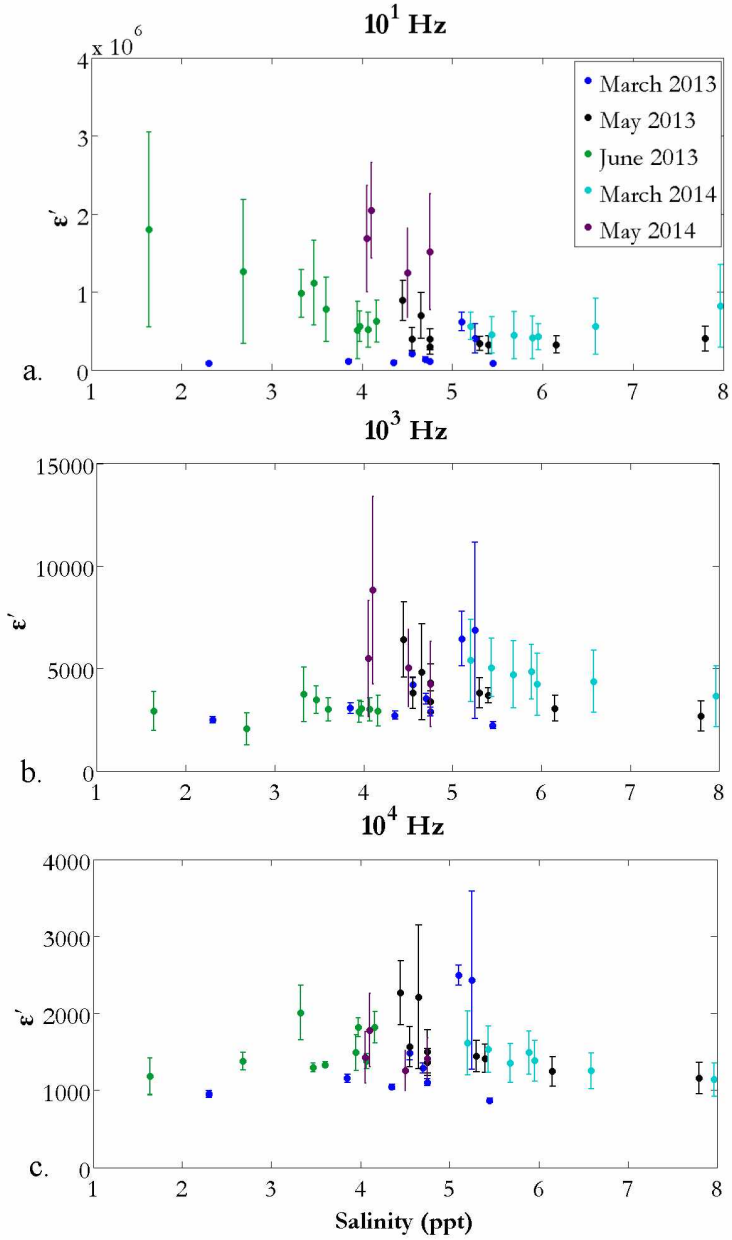

Fig. 25: Real part of the complex permittivity (ε') as a function of sea ice bulk salinity for measurements gathered in 2013 and 2014 at depths between 0.15 m to 1.05 m and frequencies of a) 10^1 Hz, b) 10^3 Hz and c) 10^4 Hz. Bars denote plus/minus one standard deviation.

Table 5: Correlation between the real part of the permittivity (ε') and salinity for measurements gathered in 2013, 2014, and 2013 and 2014 combined

	10 Hz	20 Hz	50 Hz	100 Hz	200 Hz	500 Hz	1000 Hz	2000 Hz	5000 Hz	10,000 Hz
2013	-0.54	-0.47	-0.22	-0.16	0.14	-0.15	0.22	0.15	0.09	0.08
2014	-0.65	-0.65	-0.55	-0.52	-0.58	-0.69	-0.64	-0.31	-0.57	-0.61
2013 & 2014	-0.34	-0.25	-0.10	-0.01	0.03	-0.03	0.16	0.14	-0.01	-0.05

In 2013, this correlation is found to be significant up to only 50 Hz while in 2014, correlation remains significant at frequencies up to 10,000 Hz. When the two datasets are combined, a significant correlation is found at 10 Hz. An increase in salinity results in an increase in ε' of ice (a positive relationship) given the greater likelihood of salts being included interstitially between grains. An inverse relationship exists between salinity and ε' of brine however, the result of H_2O molecules aligning with additional ions as opposed to the applied electric field. Although the correlation between ε' and bulk salinity varies in magnitude between 2013 and 2014, it is evident that neither the electric properties of ice or brine dominate measurements in either year.

To better understand this finding, the complex interchange between ice temperature, bulk salinity, and brine volume must be considered. Changes in ice temperature drive the evolution of brine volume fraction and microstructure which, in turn, can influence bulk salinity. In the winter, low ice temperature will be accompanied by small values of brine volume fraction. Drainage of high salinity brine will be prevented during this time due to low connectivity between pores. In the spring as ice temperature begins to increase, brine volume fraction will also increase and pores will connect allowing for the drainage of brine and a decrease in bulk salinity. As neither temperature nor salinity were found to control measurements of ε' entirely, brine volume fraction must also be considered. This finding is in agreement with previous studies which described, primarily qualitatively, the relationship between ε' and both brine volume fraction and other microstructural characteristics (Addison, 1970; Ingham et al., 2012).

As seen in Fig. 26 and presented in Table 6, a significant correlation between brine volume fraction is seen in 2013 at frequencies below 100 Hz.

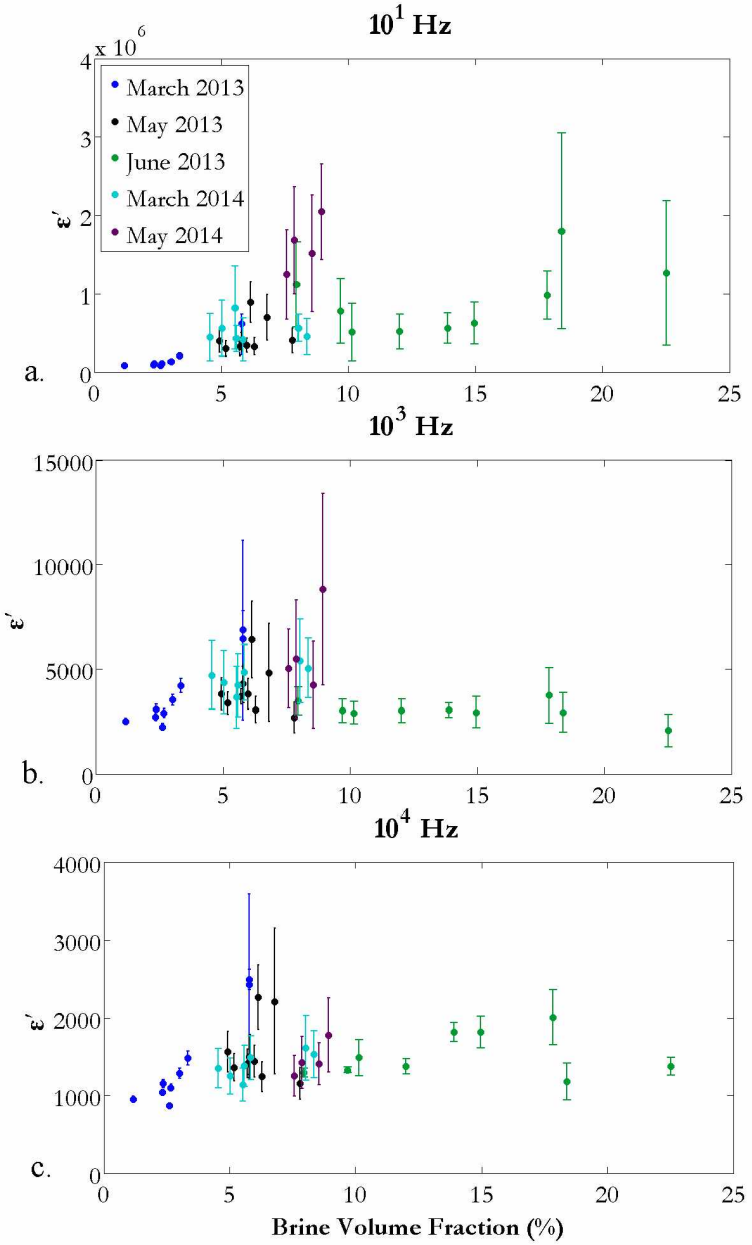

Fig. 26: Real part of the complex permittivity (ε') as a function of brine volume fraction for measurements gathered in 2013 and 2014 at depths between 0.15 m to 1.05 m and frequencies of a) 10^1 Hz, b) 10^3 Hz and c) 10^4 Hz. Bars denote plus/minus one standard deviation.

Table 6: Correlation between the real part of the permittivity (ε') and brine volume fraction for measurements gathered in 2013, 2014, and 2013 and 2014 combined.

	10 Hz	20 Hz	50 Hz	100 Hz	200 Hz	500 Hz	1000 Hz	2000 Hz	5000 Hz	10,000 Hz
2013	0.80	0.80	0.51	0.50	0.09	0.36	-0.22	0.02	0.14	0.20
2014	0.40	0.40	0.51	0.45	0.50	0.40	0.46	0.21	0.31	0.32
2013 & 2014	0.35	0.28	0.21	0.20	0.04	0.11	-0.14	0.02	0.16	0.22

In 2014, this correlation decreases but is significant at frequencies below 1000 Hz. When the two datasets are combined, a significant correlation is found below frequencies of 100 Hz. An increase in brine volume fraction accompanies an increase in temperature, both contributing to lower values of salinity as ice melts and density driven advection of brine occurs. The positive relationship found between ε' and brine volume fraction is therefore in agreement with the relationship between ε' and both temperature and salinity shown above.

5.1.2 The Imaginary Part of the Complex Permittivity

As noted previously, ε'' is representative of the overall loss, or attenuation, of the current. It is closely related to the DC conductivity of the material, which depends on the connectivity of pore spaces (Jones et al., 2012). The relationship between ε'' and ice properties remains relatively consistent across all frequencies. This is to be expected given the linear relationship displayed in Fig. 15. A significant correlation is found between ε'' and temperature (Fig. 27, Table 7), varying slightly when 2013 and 2014 are compared. Unlike ε', an increase in temperature will lead to an increase in the magnitude of ε'' for both ice and brine. The former related to the increase in the mobility of defects while for brine, a temperature increase allows ions to respond more readily to the electric field, thus increasing frictional dissipation and resultant dielectric loss.

When examining the relationship between ε'' and salinity, a significant negative correlation is found (Fig. 28, Table 8). This finding indicates that neither the individual electric properties of ice nor brine are controlling the magnitude of ε'' as both are known to display a positive correlation with salinity. The imaginary part of the complex permittivity, ε'', provides a measurement of conductive loss known to be closely tied to pore connectivity and, relatedly, brine volume fraction (Jones et al., 2012). The significant positive correlation with brine volume fraction shown in Fig. 29 and summarized in Table 9 is therefore expected. These findings indicate that ε'' of sea ice is primarily controlled by pore connectivity as opposed to the individual electric properties of ice and brine.

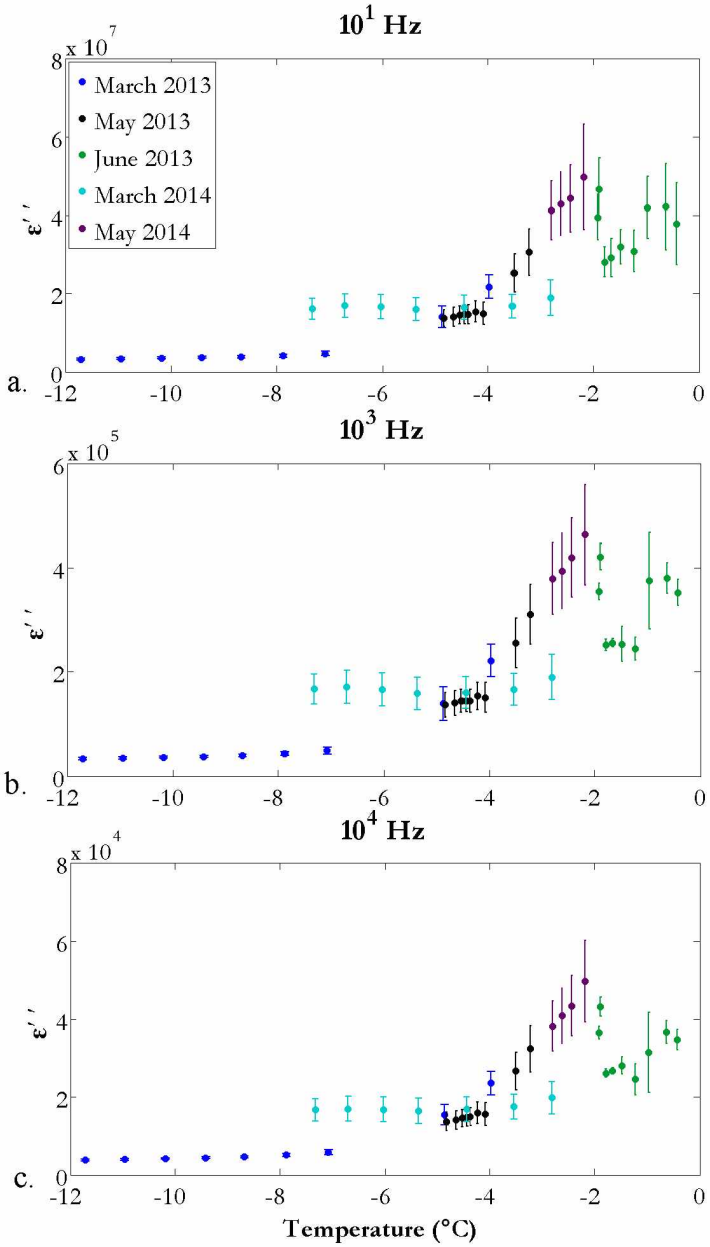

Fig. 27: Imaginary part of the complex permittivity (ε'') as a function of temperature for measurements gathered in 2013 and 2014 at depths between 0.15 m to 1.05 m and frequencies of a) 10^1 Hz, b) 10^3 Hz and c) 10^4 Hz. Bars denote plus/minus one standard deviation.

Table 7: Correlation between the imaginary part of the permittivity (ε'') and temperature for measurements gathered in 2013, 2014, and 2013 and 2014 combined.

	10 Hz	20 Hz	50 Hz	100 Hz	200 Hz	500 Hz	1000 Hz	2000 Hz	5000 Hz	10,000 Hz
2013	0.89	0.89	0.90	0.91	0.89	0.92	0.89	0.92	0.91	0.89
2014	0.72	0.72	0.72	0.74	0.72	0.70	0.72	0.71	0.73	0.74
2013 & 2014	0.79	0.79	0.78	0.79	0.76	0.76	0.76	0.76	0.77	0.77

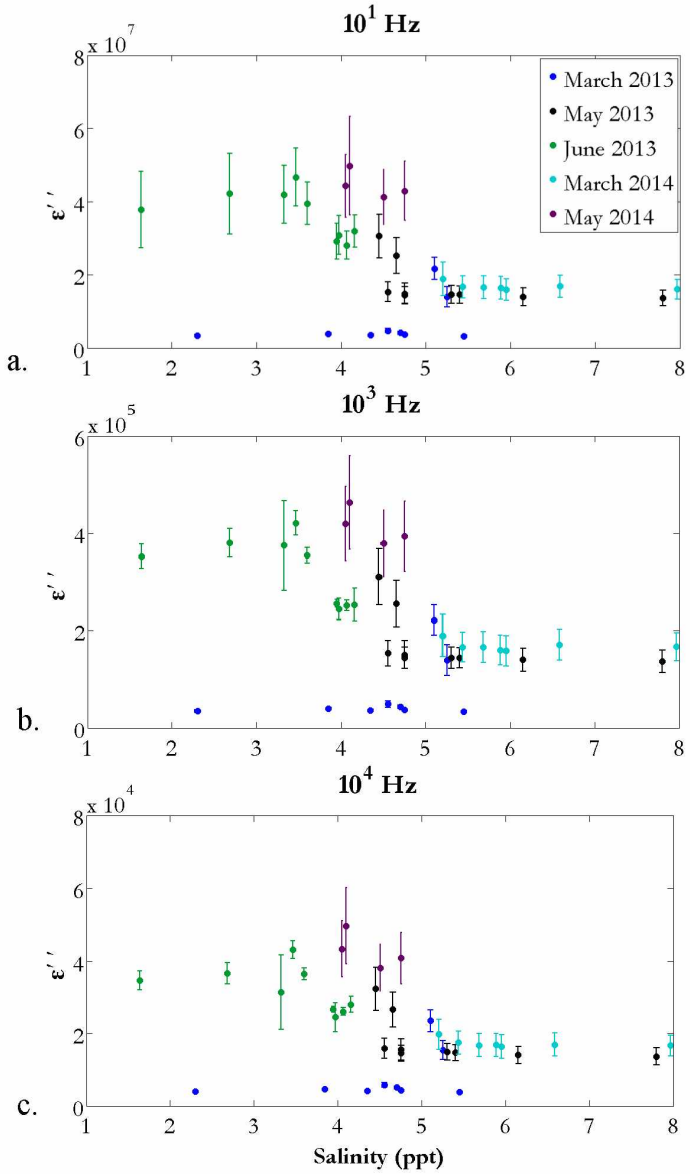

Fig. 28: Imaginary part of the complex permittivity (ε'') as a function of salinity for measurements gathered in 2013 and 2014 at depths between 0.15 m to 1.05 m and frequencies of a) 10^1 Hz, b) 10^3 Hz and c) 10^4 Hz. Bars denote plus/minus standard deviation.

Table 8: Correlation between the imaginary part of the permittivity (ε'') and salinity for measurements gathered in 2013, 2014, and 2013 and 2014 combined.

	10 Hz	20 Hz	50 Hz	100 Hz	200 Hz	500 Hz	1000 Hz	2000 Hz	5000 Hz	10,000 Hz
2013	-0.46	-0.46	-0.49	-0.44	-0.43	-0.44	-0.44	-0.44	-0.44	-0.42
2014	-0.80	-0.80	-0.80	-0.81	-0.79	-0.78	-0.80	-0.79	-0.81	-0.82
2013 & 2014	-0.40	-0.40	-0.40	-0.37	-0.36	-0.34	-0.36	-0.34	-0.36	-0.36

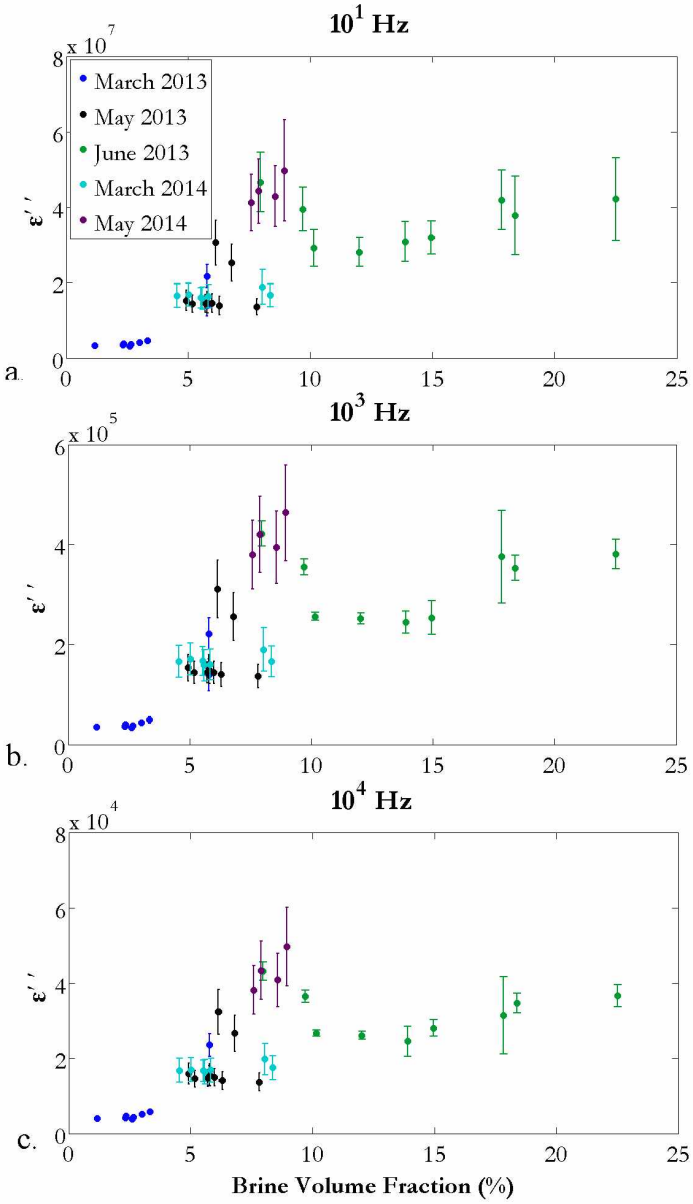

Fig. 29: Imaginary part of the complex permittivity (ε'') as a function of brine volume fraction for measurements gathered in 2013 and 2014 at depths between 0.15 m to 1.05 m and frequencies of a) 10^1 Hz, b) 10^3 Hz and c) 10^4 Hz. Bars denote plus/minus one standard deviation.

Table 9: Correlation between the imaginary part of the permittivity (ε'') and brine volume fraction for measurements gathered in 2013, 2014, and 2013 and 2014 combined.

	10 Hz	20 Hz	50 Hz	100 Hz	200 Hz	500 Hz	1000 Hz	2000 Hz	5000 Hz	10,000 Hz
2013	0.83	0.83	0.88	0.83	0.80	0.85	0.79	0.88	0.83	0.76
2014	0.53	0.52	0.51	0.55	0.51	0.49	0.51	0.50	0.54	0.56
2013 & 2014	0.61	0.61	0.63	0.59	0.55	0.56	0.55	0.57	0.56	0.53

5.2 Relationships Between Pore Microstructure and Complex Permittivity

The physical mechanisms underlying the relationship between low frequency complex dielectric permittivity and brine volume fraction of sea ice are not as easily explained in comparison to single-phase systems such as pure ice or an ionic solution. Studies focused on the low frequency behavior of a porous medium however, have revealed relationships between pore volume, connectivity, and geometry and measurements of ε' and ε'' (Scott and Barker, 2003; Nordsiek and Weller, 2008; Leroy and Revil, 2009). Results from these studies improve our understanding of the physical mechanism at play and the applicability of such methods to other porous media such as sea ice. Guided by these studies, results from the microstructural analysis are compared to measurements of complex dielectric permittivity and ice properties in the following.

5.2.1 Pore Volume Distribution

The correlations between all factors being examined in this study, including complex permittivity measurements, ice properties, and microstructural characteristics are presented in Table 10.

Table 10: Correlation matrix comparing complex permittivity at 10 Hz to all ice properties including mean pore volume (MVP), surface area to volume ratio (SA/V), depth of 25% fractional connectivity (FC), bulk brine volume fraction (Bulk BVF), sample brine volume fraction (Sample BVF), ice temperature (T), and bulk salinity (S).

	ε'	ε''	MPV	SA/V	FC	Bulk BVF	Sample BVF	T	S
ε'	1.000	0.922	0.788	-0.058	0.469	0.815	0.786	0.674	-0.239
ε''	0.922	1.000	0.836	0.008	0.654	0.894	0.793	0.835	-0.490
MPV	0.788	0.836	1.000	-0.237	0.486	0.940	0.976	0.598	-0.638
SA/V	-0.058	0.008	-0.237	1.000	-0.175	-0.018	-0.175	0.436	0.078
FC	0.469	0.654	0.486	-0.175	1.000	0.452	0.430	0.531	-0.466
Bulk BVF	0.815	0.894	0.940	-0.018	0.452	1.000	0.901	0.780	-0.629
Sample BVF	0.786	0.793	0.976	-0.175	0.430	0.901	1.000	0.593	-0.558
T	0.674	0.835	0.598	0.436	0.531	0.780	0.593	1.000	-0.504
S	-0.239	-0.490	-0.638	0.078	-0.466	-0.629	-0.558	-0.504	1.000

As only 14 samples are associated with both measurements of microstructural characteristics and complex permittivity, correlations are based on a smaller sample size than the comparison between ice properties and complex permittivity (Figs. 24-29). The correlation between complex permittivity and brine volume fraction is weaker when considering microstructural samples as opposed to bulk samples presented in Fig. 26 and Fig. 29. This is likely a reflection of heterogeneities in the ice with the small size of the microstructural samples being less then $1/10^{th}$ the size of the bulk ice samples used for ice property measurements.

Measurements of ε' were found to be most significantly correlated to brine volume fraction and mean pore volume. A principal component analysis (PCA) indicates that the loadings of mean pore volume and bulk brine volume fraction are near-equal for the first principal component and explain 52% of the variance (Table 11-13). This result indicates the potential of ε' to track not only brine volume fraction but potentially pore volume as well.

Table 11: Principal component analysis for the real part of the permittivity (ε') at 10 Hz. Loadings associated with each variable. Mean pore volume (MVP), surface area to volume ratio (SA/V), depth of 25% fractional connectivity (FC), bulk brine volume fraction (Bulk BVF), sample brine volume fraction (Sample BVF), ice temperature (T), and bulk salinity (S).

	PC1	PC2	PC3	PC4	PC5	PC6	PC7
ε'	0.326	0.255	0.706	0.486	0.077	-0.297	0.021
MPV	0.447	-0.265	0.015	-0.435	0.281	-0.380	-0.563
SA/V	-0.006	0.786	-0.381	-0.143	0.006	-0.465	0.042
FC	0.320	-0.323	-0.573	0.611	0.089	-0.255	0.134
Bulk BVF	0.488	-0.013	0.039	-0.374	0.266	0.125	0.731
T	0.443	0.376	-0.165	0.160	0.117	0.685	-0.357
S	-0.397	0.042	0.004	0.123	0.907	0.046	-0.009

Table 12: Principal component analysis for the imaginary part of the permittivity at 10 Hz. Loadings associated with each variable. Mean pore volume (MVP), surface area to volume ratio (SA/V), depth of 25 % fractional connectivity (FC), bulk brine volume fraction (Bulk BVF), sample brine volume fraction (Sample BVF), ice temperature (T), and bulk salinity (S).

	PC1	PC2	PC3	PC4	PC5	PC6	PC7
ε''	0.420	0.155	0.039	-0.005	0.786	-0.425	0.018
MPV	0.425	-0.264	-0.352	0.321	-0.315	-0.318	-0.568
SA/V	0.000	0.819	0.084	0.043	-0.388	-0.411	0.038
FC	0.314	-0.297	0.838	0.076	-0.245	-0.170	0.129
Bulk BVF	0.466	-0.014	-0.335	0.292	-0.161	0.154	0.732
T	0.428	0.382	0.185	0.100	0.077	0.704	-0.352
S	-0.379	0.043	0.141	0.891	0.202	0.017	-0.008

Table 13: Variance associated with each principal component.

Principal Component	Fraction of variance explained (%), ε'	Fraction of variance explained (%), ε''
1	52.1	56.6
2	19.9	19.6
3	10.5	9.3
4	8.7	7.2
5	7.2	5.9
6	1.4	1.2
7	0.3	0.3

To further examine this finding, ε' and ε'' are compared to mean pore volume in Fig. 30. Similar to the above analysis examining the impact of BVF on ε'', the correlation between ε'' and pore volume is expected given its relationship of pore connectivity. In processing of images, brine pores, layers, and channels were not differentiated; therefore, a large "pore" may be associated with a well-connected brine channel. As mean pore volume increases, so too will the connectivity of pore spaces. More pathways will therefore be available for current to travel, increasing conductivity and related values of ε''. This relationship is further supported by the significant correlation found between fractional connectivity and pore volume presented in Table 10.

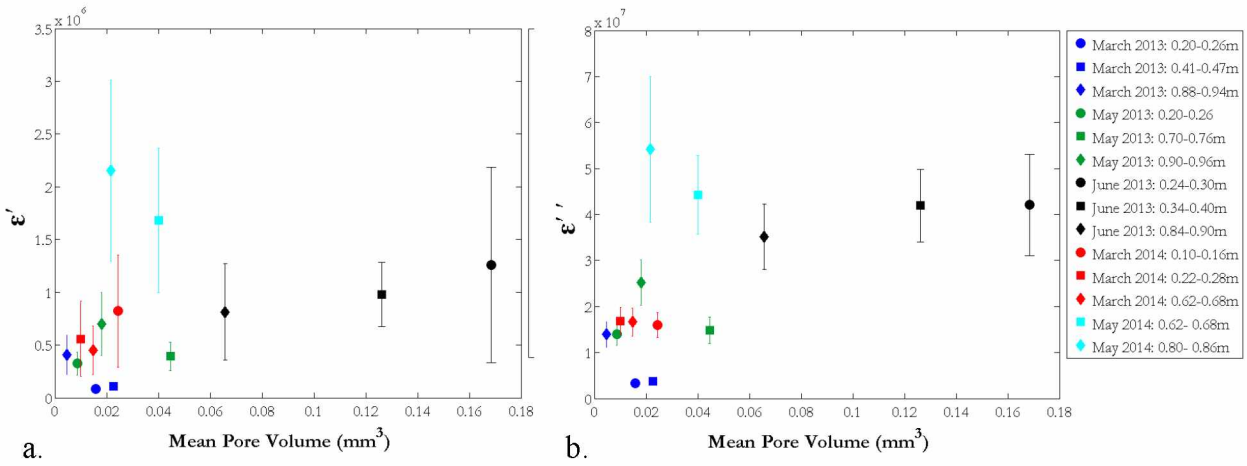

Fig. 30: Comparison of complex permittivity to mean pore volume based on 14 microstructural samples gathered in 2013 and 2014. Bars representative of one standard deviation. (a) ε' and (b) ε''.

The relationship between ε', brine volume fraction, and mean pore volume is more complicated. The rise in ε' at low frequencies has been examined in studies of composite media (Buchanan et al., 2011; Kemna et al., 2012; Bücker and Hördt, 2013). In application to both sea ice and other porous media, space charge polarization is labeled as the primary cause for this increase apparent below frequencies of 1000 Hz. Dielectric polarization, responsible for values of ε_∞ and ε_s for homogeneous materials, is associated with charge separation on an atomic or molecular scale. Space charge polarization on the other hand, is a broad term associated with the greater separation of mobile charge carriers when an electric field is applied. As a result the magnitude of ε' associated with space charge processes is often much greater than that of dielectric polarization (Macdonald, 1953). In the sea ice system, space charge polarization is challenging to estimate given the constant variation in the proportion of ice to brine and their contrasting electric properties (Addison, 1970). When a low frequency alternating current is applied, ions within the brine will separate based on charge, creating a gradient in concentration that leads to the diffusion of ions to re-establish balance. At higher frequencies, there is not enough time for this to occur (M. Ingham, Personal Communication, 2014; Macdonald, 1953; Titov et al., 2002). Depending on the size of the pore, the time needed for diffusive dissipation to occur will differ. Larger pores will therefore show relaxations at lower frequencies with longer periods.

In a traditional Cole-Cole model, a single relaxation time is assigned to space charge polarization effects. More recent studies however, have begun to examine this relaxation at low frequencies as a sum of relaxations associated with pores of varying sizes. Debye decomposition, summarized in the Background section, uses an alternate approach to the Cole-Cole and associated models, fitting a spectrum of Debye relaxations to measurements in order to determine the amount of chargeability associated with a given relaxation time (Nordsiek and Weller, 2008). In the process of conducting the above analysis, this method was examined briefly using modeled values of ε* at frequencies below 10 Hz. Results were promising, showing a trend towards greater chargeability associated with lower frequency relaxations and hence larger pores as ice evolved from March through June. Such findings are in good agreement with results of pore volume distribution presented above. Given the exploratory nature of this work, however, the approach and resultant data need further examination before being presented.

The results shown in Fig. 31, reveal a significant linear relationship between BVF and mean pore volume, however, no distinction between granular and columnar layers is apparent. From these findings one might be able to develop a general relationship linking the two properties. The result would allow for estimation of microstructural characteristics when only measurements of brine volume fraction are available.

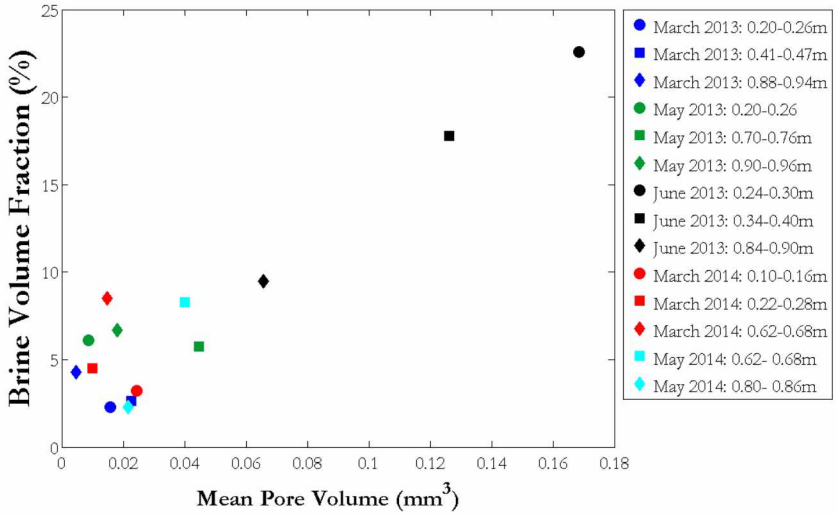

Fig. 31: Comparison of bulk brine volume fraction to mean pore volume based on 14 microstructural samples gathered in 2013 and 2014.

5.2.2 Fractional Connectivity

Connectivity was found to be significantly correlated with both ε' and ε'', contributing equally to both first principal components but of lesser magnitude than mean pore volume (Table 9 and 10). The relationship between ε'' and connectivity shown in Fig. 30 is well established for laboratory grown and modeled sea ice (Pringle et al., 2009; Jones et al., 2010). The data presented here expand on previous findings and reveal a similar relationship in natural sea ice. The correlation found between fractional connectivity and ε', is likely driven by the relationship between connectivity, brine volume fraction, and pore volume. While a correlation is present, however, inconsistencies are found in the data particularly in June of 2013. During this time, the magnitudes of ε' and ε'' were uniform throughout the depth of the ice. This is unexpected given a strong variation in both fractional connectivity and mean pore volume as depth increases. While values for mean pore volumes between granular and columnar ice vary, the general distribution of pores is similar in upper and lower layers of June 2013 ice (Fig. 21). The biggest difference is only apparent in pores >10 mm^3 with lower layers having no pores of this volume despite greater fractional connectivity. The little variation found in measurements of ε' and ε'' taken in June 2013 despite microstructural differences may also be a reflection of permittivity measurements being taken in the horizontal as opposed to vertical direction. Pore connectivity in either direction will impact conductive loss. Uniformity in measurements of both ε' and ε'' may therefore be the result of differences in horizontal and vertical connectivity found in granular versus columnar layers.

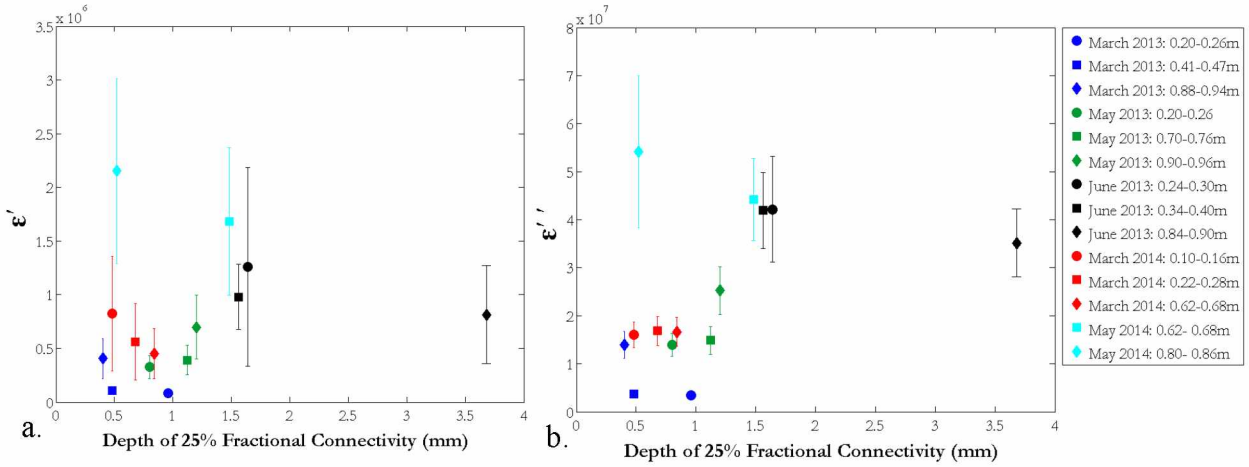

Fig. 32: Comparison of complex permittivity to the depth of 25 % fractional connectivity based on 14 microstructural samples gathered in 2013 and 2014. Bars denote plus/minus one standard deviation. (a) ε' and (b) ε''.

When examining measurements of fractional connectivity in relationship to brine volume fraction, a depth dependence is apparent (Fig. 33). At values of brine volume fraction around 5 %, depth of 25 % fractional connectivity varies slightly between 0.5 mm to 1.5 mm. Despite having similar values of brine volume fraction, values obtained in upper granular layers show lesser values of fractional connectivity. This trend is particularly apparent in June of 2013 where samples gathered immediately below and above the transition layer (at 0.30 m) show greater brine volume fraction but lesser fractional connectivity than the sample gathered in ice where columnar structure was well established. These findings suggest that brine volume fraction, while offering a convenient method to track general evolution of ice, is not equally represented in granular and columnar ice in terms of connectivity. Examining initial results in Fig. 20, the difference in the evolution of fractional connectivity in granular vs. columnar layers is even more apparent. While granular layers remained disconnected from the top to bottom, the lower, columnar layers displayed a gradual evolution towards full connectivity. Therefore, after further examination of the impacts discussed above, measurements of ε'' may offer a more accurate method to track connectivity and predict the onset of percolation. Additionally, such measurements when used in combination with estimates of brine volume fraction and/or pore volume may enable the identification of ice texture without removal of cores.

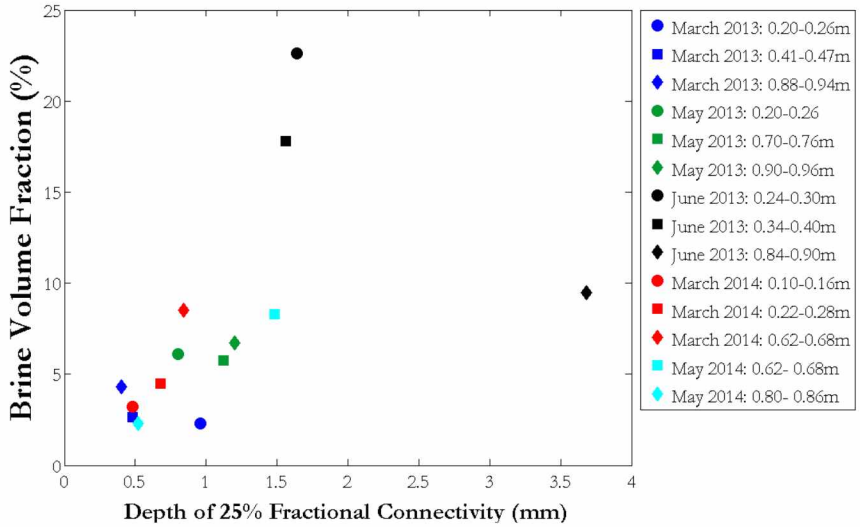

Fig. 33: Comparison of bulk brine volume fraction to depth of 25 % fractional connectivity based on 14 samples gathered in 2013 and 2014.

5.2.3 Surface Area to Volume Ratio

Results shown in Fig. 34 show no significant correlation between SA/V ratio and ε' or ε'' (Table 9). When examining results from the PCA, however, SA/V ratio is found to be the dominant factor controlling the second component responsible for 20 % of the variance seen between all measurements (Table 11). SA/V ratio was chosen given its potential to possibly track the formation of pore necks within pores. Such features further complicate pore geometry presumably increasing SA/V ratio. Pore necks are believed to give rise to membrane polarization. This process occurs in pore necks where an electric double layer has formed thus repelling ions of equivalent charge and leading to a smaller fraction of such ions to pass through. A depletion of ions on one side of the neck will result (Kemna et al., 2012). Addison, (1970) mentioned this process in his initial study of sea ice, holding it accountable for one pore containing a narrow neck to behave as two separate pores.

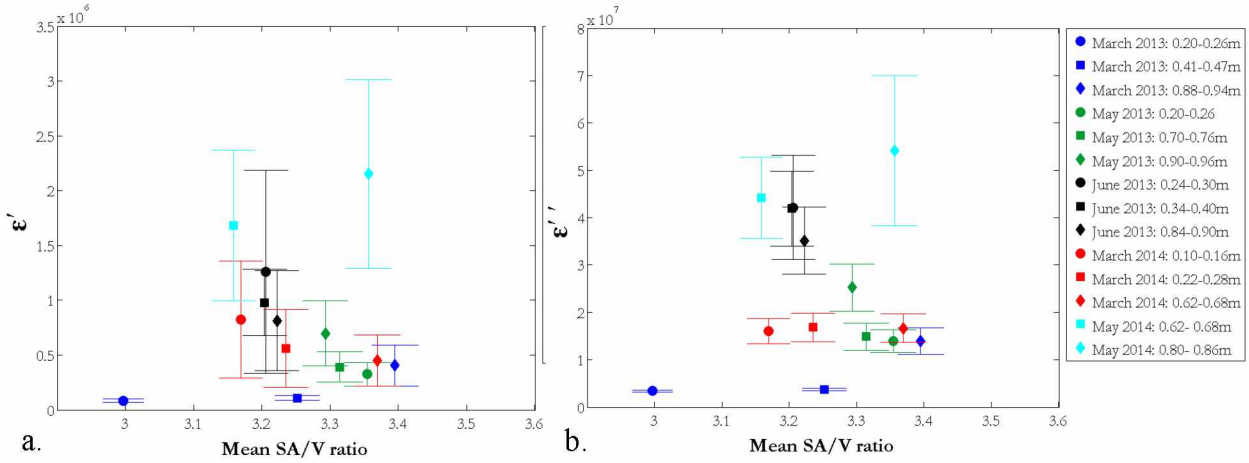

Fig. 34: Comparison of complex permittivity to mean SA/V ratio based on 14 microstructural samples gathered in 2013 and 2014. Bars denote plus/minus one standard deviation. (a) ε' and (b) ε''.

When examining results presented in Fig. 22, an evolution in microstructure is apparent. In March, there is a larger spread in values of SA/V ratio relative to total brine volume fraction possibly indicative of small pores connected only through narrow necks. As ice warms, a greater proportion of pores with lower SA/V ratios are created. In 2013 and 2014 ice, measurements of SA/V gathered in May show a broad distribution of SA/V ratios alluding to greater variation in pore geometry. By June, the majority of pores show low values of SA/V ratio indicative of the larger, well connected pore space that previous analysis has shown.

When examining results of the principal component analysis, SA/V ratio had the greatest loading in comparison to all other variables for the second principal component responsible for 20 % of variance. Therefore, while a relationship to complex permittivity is not initially apparent, measurements of electric properties may provide a method to track SA/V ratio. Complex conductivity, for instance, has been found to be sensitive to the smoothness and distribution of mineral grains (Leroy and Revil, 2009). This relationship is linked to processes occurring outside and inside the electric double layer contributing to values of real and imaginary parts of the complex conductivity; discussion of these processes is outside the scope of this thesis. Results from Leroy and Revil's (2009) study show a strong relationship between the phase of the complex conductivity and the smoothness and distribution of grains. The evolution of brine pores' SA/V ratio presented in Fig. 22 offers a similar scenario where complex conductivity measurements may prove useful.

Chapter 6: Conclusions

While the low frequency electric properties of sea ice first became a topic of study in the late 1960s it was not until recently that their use as a method to track microstructural evolution has been explored in depth. Studies including that by Buchanan et al. (2011) provided a thorough examination of measurements in the frequency range of 40 Hz to 1 MHz, subsequently applying conductive-dielectric models to results to derive estimates of brine pore size and orientation. A complete description of sea ice microstructure could not be obtained, however, in this laboratory study of an oversimplified sea-ice system. The research presented here applied methods established by Buchanan et al. (2011) but took a separate approach to link findings to microstructure. Focus was placed on the dielectric permittivity of natural sea ice and relationships to ice temperature, bulk salinity, and microstructure were explored and quantified. This dataset, the first of its kind to our knowledge, offers a detailed look at the seasonal evolution of natural sea ice, providing new insight into interrelations between factors influencing the electric properties of sea ice.

6.1 Key Findings

The physical mechanisms controlling the electric response of sea ice are reflected in the relationships found between ice properties, microstructure, and the complex dielectric permittivity. Results from this study therefore provide quantitative evidence that complex dielectric permittivity is largely controlled by and therefore capable of tracking the evolution of microstructural characteristics. The significant correlation found between brine volume fraction and the real part of the dielectric permittivity is in agreement with theoretical conclusions attributing the low frequency response of sea ice to space charge polarization and interfacial effects. This finding is further supported when temperature and salinity are compared to measurements of the real part of the permittivity. While the correlations with these two ice properties are significant, they indicate that neither ice nor brine dominates the electric response of sea ice. Further examination of the real part of the permittivity revealed a significant correlation with pore volume as well, suggesting that the distribution of brine within the ice matrix, and not simply the amount, largely influences measurements. The imaginary part of the dielectric permittivity was also significantly correlated with brine volume fraction, a reflection of its relationship to DC conductivity and pore connectivity established in previous studies.

The microstructural characterization considered independently, provides a more detailed examination of the seasonal evolution of natural sea ice and variations present from year to year. Such results may improve understanding of the causes of microstructural variations and their possible impact on hydraulic properties, the movement of oil in ice, and the distribution and abundance of microbiota. In addition, results showed relationships between brine volume fraction and other microstructural characteristics that are more challenging to measure. Mean pore volume and brine volume fraction displayed a strong linear relationship. Connectivity however, while strongly correlated with brine volume fraction at low values, showed sensitivity to ice texture once brine volume fraction increased above 5 %. In addition, surface area to volume ratio of pore spaces showed no strong correlation to either dielectric permittivity or brine volume fraction but displayed a clear seasonal evolution from March to June in 2013 and 2014.

6.2 Directions for Future Work

While measurements of dielectric permittivity offer promise in the development of methods to track the seasonal evolution of sea ice microstructure *in situ* and continuously, further work is needed to support and expand the findings presented here. Focus must be placed primarily on sea ice of brine volume fractions greater than 5 %. As shown in Figs. 24-29, above this value the standard deviation as well as the difference between 2013 and 2014 measurements increased substantially. A 5 % brine volume fraction is thought of as a threshold above which the pore connectivity of sea ice is typically large enough to enable percolation. It signifies a microstructural transition causing greater heterogeneity within the ice and increasing the number of variables possibly impacting electric measurements. Additionally, as brine volume fraction further increases to values seen in June ($\geq$ 10 %), a greater amount of brine is present in the system and possibly in contact with electrodes. When high brine volumes are widespread, electrode polarization is evident in electric permittivity measurements. The magnitude of this effect and its impact on specific electrodes is difficult to determine however. To address this source of error, it is recommended that estimations of brine permittivity at low frequencies should be further examined. While measurement may be complicated, through experimentation and modeling, estimations for the complex permittivity of brine at varying temperatures and salinity would allow for specific bounds to be placed on electrode polarization. Findings would

be useful in future modeling of complex permittivity data to better account for electrode polarization versus space charge effects.

To apply the methods developed in studies of spectral induced polarization and develop microstructural models applicable to sea ice, measurements must be gathered at frequencies below 10 Hz. The approaches briefly summarized including Debye decomposition require values for complex permittivity at mHz frequencies. While such data can be obtained through the application of a Cole-Cole model, this method introduces a substantial amount of error, deriving values for upwards of 7 parameters. Measurement at lower frequencies will therefore decrease error in addition to enabling further exploration of micro-scale physical mechanisms at work. As a result, a greater understanding of the prominent factors impacting permittivity measurements in, specifically, a sea ice volume can be gained.

6.3 Perspective

By following these recommendations, development of a model capable of accurately deriving key microstructural characteristics of sea ice from complex permittivity measurements is possible. Perhaps the most relevant characteristic to be targeted first, and for which this study has established well-defined relationships to permittivity, is brine volume fraction. Given its use in a number of applications a method to monitor brine volume fraction continuously and *in situ* will lead to an improved understanding of sea ice evolution and its impact on the surrounding environment. Measurement of mean pore volume, fractional connectivity, and SA/V ratio may increase the accuracy of these established relationships. Additionally, knowledge of the evolution of specific microstructural characteristics may prove useful in studies unassociated with the physical properties of the ice. The presence and concentration of biota within the ice, for instance, is largely influenced by the size and geometry of pore spaces and channels which provide microbiota protection from scavengers while supplying them nutrients (Krembs et al., 2000). The study of oil in sea ice, increasing in its importance, may also benefit from such measurements given their ability to track microstructural evolution on a more detailed level. While approximations based primarily on the brine volume fraction necessary for percolation upward exist (Karlsson et al., 2011), improvements need to be made before accurate models are created. Having an improved understanding of microstructural evolution of natural sea ice

including the connectivity of pore space through the ice, the complexity of pathways, and the shape of pores will prove useful as this topic is further examined.

The research conducted as part of this thesis provides a dataset linking the low frequency dielectric properties of natural sea ice to microstructure and ice properties. Results suggest that measurement of the low frequency dielectric permittivity offer a method to monitor sea ice microstructure *in situ* and continuously thus improving our current observations of the sea ice system as a whole. In addition, these findings provide a base of knowledge applicable to a variety of studies and further contribute to our understanding of sea ice processes on both the macro- and micro-scale.

Works Cited:

Addison JR (1969) Electrical properties of saline ice. *J. Appl. Phys.* 40(8), 3105–3114

Addison JR (1970) Electrical relaxation in saline ice. *J. Appl. Phys.* 41(1), 54–63

Arcone SA, Gow AJ and McGrew S (1986) Structure and dielectric properties at 4.8 and 9.5 GHz of saline ice. *J. Geophys. Res.* 91(C12), 14281 (doi:10.1029/JC091iC12p14281)

Arctic Council (2009). *Arctic Marine Shipping Assessment 2009 Report*. Arctic Council, Norwegian Chairmanship, Oslo, Norway

Backstrom LGE and Eicken H (2006) Capacitance probe measurements of brine volume and bulk salinity in first-year sea ice. *Cold Reg. Sci. Technol.* 46(3), 167–180 (doi:10.1016/j.coldregions.2006.08.018)

Buchanan S, Ingham M and Gouws G (2011) The low frequency electrical properties of sea ice. *J. Appl. Phys.* 110(7), 1–10 (doi:10.1063/1.3647778)

Bücker M and Hördt A (2013) Analytical modelling of membrane polarization with explicit parametrization of pore radii and the electrical double layer. *Geophys. J. Int.* 194(2), 804–813 (doi:10.1093/gji/ggt136)

Chaplin M (2014) Water and Microwaves. *Water Structure and Science*. Creative Commons Attribution, 18 Dec. 2014. Web. Jan 2015. http://www1.lsbu.ac.uk/water/microwave_water.html

Cox GFN and Weeks WF (1983) Equations for determining the gas and brine volumes in sea-ice samples. *J. Glaciol.* 29(102), 306–316

Druckenmiller ML, Eicken H, Johnson MA, Pringle DJ and Williams CC (2009) Toward an integrated coastal sea-ice observatory: System components and a case study at Barrow, Alaska. *Cold Reg. Sci. Technol.* 56(2-3), 61–72 (doi:10.1016/j.coldregions.2008.12.003)

Eicken H, Krouse HR, Kadko D and Perovich DK (2002) Tracer studies of pathways and rates of meltwater transport through Arctic summer sea ice. *J. Geophys. Res. Ocean.* 107(C10), SHE–22

Fetterer F, Knowles K, Meier W, and Savoie M (2002) Updated daily. *Sea Ice Index*. Boulder, Colorado USA: National Snow and Ice Data Center (doi: 10.7265/NFQJ7F7W).

Golden KM, Ackley SF and Lytle VI (1998) The percolation phase transition in sea ice. *Science* 282(5397), 2238–2241

Gradinger R, Spindler M and Weissenberger J (1992) On the structure and development of Arctic pack ice communities in Fram Strait: a multivariate approach. *Polar Biol.* 12(8), 727–733

Grimm RE, Stillman DE, Dec SF and Bullock MA (2008) Low-frequency electrical properties of polycrystalline saline ice and salt hydrates. *J. Phys. Chem. B* 112(48), 15382–15390 (doi:10.1021/jp8055366)

Hallikainen M and Winebrenner DP (1992) The physical basis for sea ice remote sensing. *Microwave Remote Sensing of Sea Ice*, 29–46. American Geophysical Union. (10.1029/GM068p0029)

Hasted JB (1973) *Aqueous dielectrics.* Chapman and Hall, London

Ingham M, Gouws G, Buchanan S, Brown R and Haskell T (2012) In-situ measurements of the low frequency dielectric permittivity of first-year Antarctic sea ice. *Cold Reg. Sci. Technol.* 83-84, 139–146 (doi:10.1016/j.coldregions.2012.07.008)

Ingham M, Pringle D and Eicken H (2008) Cross-borehole resistivity tomography of sea ice. *Cold Reg. Sci. Technol.* 52(3), 263–277 (doi:10.1016/j.coldregions.2007.05.002)

Eide L and Martin S (1975) The formation of brine drainage features in young sea ice. *J. Glaciol.* 14, 137–154

Jones KA, Ingham M and Eicken H (2012) Modeling the anisotropic brine microstructure in first-year Arctic sea ice. *J. Geophys. Res. Ocean.* 117(2), 1–14 (doi:10.1029/2011JC007607)

Jones KA, Ingham M, Pringle DJ and Eicken H (2010) Temporal variations in sea ice resistivity: Resolving anisotropic microstructure through cross-borehole DC resistivity tomography. *J. Geophys. Res. Ocean.* 115(11), 1–14 (doi:10.1029/2009JC006049)

Junge K, Imhoff F, Staley T and Deming W (2002) Phylogenetic diversity of numerically important Arctic sea-ice bacteria cultured at subzero temperature. *Microb. Ecol.* 43(3), 315–328

Karlsson J, Petrich C and Eicken H (2011) POAC '11: Oil Entrainment and Migration in Laboratory-grown Saltwater Ice. *Proc. 21st Int. Conf. Port Ocean Eng. under Arct. Cond.* (AMSA 2009), 1–10

Kemna A, Binley A, Cassiani G, Niederleithinger E, Revil A, Slater L, Williams KH, Orozco AF, Haegel F-H and Hoerdt A (2012) An overview of the spectral induced polarization method for near-surface applications. *Near Surf. Geophys.* 10(6), 453–468

Krembs C, Gradinger R and Spindler M (2000) Implications of brine channel geometry and surface area for the interaction of sympagic organisms in Arctic sea ice. *J. Exp. Mar. Bio. Ecol.* 243(1), 55–80

Langhorne PJ and Robinson WH (1986) Alignment of crystals in sea ice due to fluid motion. *Cold Reg. Sci. Technol.* 12(2), 197–214

Leppäranta M and Manninen T (1988) The brine and gas content of sea ice with attention to low salinities and high temperatures. *Finnish Inst. Mar. Res. Intern. Rep.* 88(2)

Leroy P and Revil A (2009) A mechanistic model for the spectral induced polarization of clay materials. *J. Geophys. Res. Solid Earth* 114(10), 1–21 (doi:10.1029/2008JB006114)

Macdonald JR (1953) Theory of ac space-charge polarization effects in photoconductors, semiconductors, and electrolytes. *Phys. Rev.* 92(1), 4–17 (doi:10.1103/PhysRev.92.4)

Malmgren F (1927) On the properties of sea-ice. *Scientific Results of the Norwegian North Pole Expedition "Maud" 1918- 1925* 1(5), 1-67

Milton GW (1981) Bounds on the complex permittivity of a two-component composite material. *J. Appl. Phys.* 52(8), 5286–5293

Moore JC and Fujita S (1993) Dielectric properties of ice containing acid and salt impurity at microwave and low frequencies. *J. Geophys. Res.* 98(B6), 9769 (doi:10.1029/93JB00710)

Morey RM, Kovacs A and Cox GFN (1984) Electromagnetic Properties of Sea Ice. *Cold Reg. Sci. Technol.* 9(9), 53–75

Nordsiek S and Weller A (2008) A new approach to fitting induced-polarization spectra. *Geophysics* 73(6), F235–F245

Notz D and Grae Worster M (2008) In situ measurements of the evolution of young sea ice. *J. Geophys. Res. Ocean.* 113(3), 1–7 (doi:10.1029/2007JC004333)

Ono N (1968) Thermal properties of sea ice. Part 4- Thermal constants of sea ice (Sea ice model calculation of thermal conductivity and diffusivity), 329–349

Pelton WH, Sill WR and Smith BD (1983) Interpretation of complex resistivity and dielectric data, Part I. *Geophys. Trans.* 29(4), 297–330

Pelton WH, Ward SH, Hallof PG, Sill WR and Nelson PH (1978) Mineral discrimination and removal of inductive coupling with multifrequency IP. *Geophysics* 43(3), 588–609

Perovich DK and Gow AJ (1996) A quantitative description of sea ice inclusions. *J. Geophys. Res.* 101(C8), 18327 (doi:10.1029/96JC01688)

Petrenko VF and Whitworth RW (1999) *Physics of ice.* Oxford University Press, New York, New York

Petrich C (2012) Sea Ice Break-Up Forecast for Barrow, Alaska. *Sea Ice Group at the Geophysical Institute.* Web. January 2015. http://seaice.alaska.edu/gi/observatories/barrow_breakup

Petrich C and Eicken H (2010) Growth, Structure and Properties of Sea Ice, in Thomas, DN and GS Dieckmann (eds.) *Sea Ice*, 23–78. Wiley-Blackwell. (doi:10.1002/9781444317145.ch2)

Pringle DJ, Miner JE, Eicken H and Golden KM (2009) Pore space percolation in sea ice single crystals. *J. Geophys. Res. Ocean.* 114(12), 1–14 (doi:10.1029/2008JC005145)

Schwerdtfeger P (1963) The thermal properties of sea ice. *J. Glaciol.* 4, 789–807

Scott JBT and Barker RD (2003) Determining pore-throat size in Permo-Triassic sandstones from low-frequency electrical spectroscopy. *Geophys. Res. Lett.* 30(9) 1450

Seigel H, Nabighian M, Parasnis DS and Vozoff K (2007) The early history of the induced polarization method. *Leading Edge* 26(3), 312–321

Titov K, Komarov V, Tarasov V and Levitski A (2002) Theoretical and experimental study of time domain-induced polarization in water-saturated sands. *J. of Appl. Geophys.* 50(4), 417–433

Untersteiner N (1968) Natural desalination and equilibrium salinity profile of perennial sea ice. *J. Geophys. Res.* 73(4), 1251–1257

Vant MR, Ramseier RO and Makios V (1978) The complex-dielectric constant of sea ice at frequencies in the range 0.1–40 GHz. *J. Appl. Phys.* 49(3), 1264–1280

Van Voorhis GD, Nelson PH and Drake TL (1973) Complex resistivity spectra of porphyry copper mineralization. *Geophysics* 38(1), 49–60

Weeks WF and Ackley SF (1982) *The Growth, Structure, and Properties of Sea Ice.* Cold Regions Research and Engineering Laboratory (U.S.). *CRREL monograph* 82-1. Hanover, NH.

Worster MG and Wettlaufer JS (1997) Natural convection, solute trapping, and channel formation during solidification of saltwater. *J. Phys. Chem. B* 101(32), 6132–6136 (doi:10.1021/jp9632448)

Zisser N, Kemna A and Nover G (2010) Relationship between low-frequency electrical properties and hydraulic permeability of low-permeability sandstones. *Geophysics* 75(3), E131–E141

Appendix : Matlab Code for Processing Microtomography Image

```
clear all; close all; clc;
```

Read in images

```
fileFolder2=fullfile('/Volumes','MegO Backup','megan','2014','201405xx','80_86','take2','recon2');%Using images saved on "Kingston". Will need to be altered
dirOutput2 = dir(fullfile(fileFolder2,'201405xx-80_86-mf-na-_rec*.jpg'));
fileNames2 = {dirOutput2.name}';
```

Create ROI

```
%Click to create corners of polygon. Double click when finished.

getimage=imread(fileNames2{200});
ROI=roipoly(getimage(:,:,1));
close all
ROI=uint8(ROI);
Index exceeds matrix dimensions.

Error in Code_for_Appendix (line 16)
getimage=imread(fileNames2{200});
```

Smooth

```
% create 3D matrix from individual images
for a=1:(length(fileNames2)-1);
   origin2=imread(fileNames2{a});
   grayscale_img(:,:,a)=origin2(:,:,1);
end

%Apply average filter vertically over three slices (1x3 kernel)
avg_filter(:,:,1)=[1/27 1/27 1/27; 1/27 1/27 1/27; 1/27 1/27 1/27];
avg_filter(:,:,2)=[1/27 1/27 1/27; 1/27 1/27 1/27; 1/27 1/27 1/27];
avg_filter(:,:,3)=[1/27 1/27 1/27; 1/27 1/27 1/27; 1/27 1/27 1/27];

smoothgray_avg=imfilter(grayscale_img, avg_filter,'replicate');

smoothgray=smoothgray_avg;
```

Load and create 3d binary matrix

```
%Thresholds for ice/air determined through a maximum likelihood classification.
%Threshold for ice/brine from close examination of images given minimal amount of brine in samples

%imhist(smoothgray(:,:,200),(256*10));  %for individual examination

level1=91/256;  %air/ice
level2=160/256;  %ice/brine

%%Binarize slice using thresholds defined above
for c=1:(length(fileNames2)-2);
%    origin=imread(fileNames2{n});
%    origin2=origin(:,:,1);

   smoothgrayROI=smoothgray(:,:,c).*ROI;
   stack(:,:,c)=smoothgrayROI;
   stackbw1(:,:,c)=im2bw(stack(:,:,c),level1); %set air pore spaces to 0
   stackbw1(:,:,c)=~stackbw1(:,:,c);
```

```
    stackbw1(:,:,c)=uint8(stackbw1(:,:,c)).*ROI;
    stackbw2(:,:,c)=im2bw(stack(:,:,c),level2);%set all but brine pore spaces to 0

end

%set both air and brine pores equal to zero
stackbw= stackbw1+stackbw2;

%set all area outside to ROI to zero
for d=1:(length(fileNames2)-2);
    stackbw3(:,:,d)=stackbw(:,:,d).*double(ROI);
end

%create logical array
stackbw3=logical(stackbw3);
```

Find Distribution of Horizontal Widths of Pore Spaces

```
%Find all connected objects (aka- pores)
CC_volume=bwconncomp(stackbw3,26);
sizeVOL=CC_volume.NumObjects;  %define volume
[xdim,ydim,zdim]=size(stackbw3); %define x,y,z coordinates for each voxel for each object
dims=[xdim ydim zdim];

%Find extent of each object in x,y, and z directions.
%Determine major/minor axis length, orientation, perimeter, equivalent diameter
%at for each horizontal slice for each object
for i = 2:sizeVOL
    clear zmin zmax a b c xmin xmax ymin ymax xext yext sz resubx resuby indxy slice sliceprops volx sliceSAV
sliceprops2
    [x,y,z]= ind2sub(dims, cell2mat(CC_volume.PixelIdxList(1,i)));
    zmin=min(z); zmax=max(z);
    zext(1,i-1)=(zmax-zmin)+1;
    for j=0:(zext(1,i-1)-1);
        a= find(z==zmin+j);
        b= x(a); c=y(a);
        xmin(1,j+1)=min(b); xmax(1,j+1)=max(b);
        ymin(1,j+1)=min(c); ymax(1,j+1)=max(c);
        xext(1,j+1)=(xmax(1,j+1)-xmin(1,j+1))+1; yext(1,j+1)=(ymax(1,j+1)-ymin(1,j+1))+1;
        slice=zeros(xext(1,j+1), yext(1,j+1));
        sz=[xext(1,j+1) yext(1,j+1)];
        resubx=(b-xmin(1,j+1))+1; resuby=(c-ymin(1,j+1))+1;
        indxy=sub2ind(sz,resubx,resuby);
        slice(indxy)=1;

sliceprops{1,j+1}=regionprops(slice,'MajorAxisLength','MinorAxisLength','Orientation','Perimeter','EquivDiameter'
);
        volx (1,j+1)=length(a);
        sliceSAV(1,j+1)=sliceprops{1,j+1}.Perimeter/volx(1,j+1);
        sliceprops2(1,j+1)=sliceprops{1,j+1}.MajorAxisLength;
        sliceprops2(2,j+1)=sliceprops{1,j+1}.MinorAxisLength;
        sliceprops2(3,j+1)=sliceprops{1,j+1}.Orientation;
        sliceprops2(4,j+1)=sliceprops{1,j+1}.Perimeter;
        sliceprops2(5,j+1)=sliceprops{1,j+1}.EquivDiameter;
        sliceprops2(6,j+1)=xext(1,j+1); sliceprops2(7,j+1)=yext(1,j+1);
```

```
    end

    finalSP{1,i-1}=sliceprops2;


end

for e=1:length(finalSP);
    min_minoraxis(1,e)=min(finalSP{1,e}(2,:));
end

% Define row,column,depth for each part of connected object for volume
w3=xdim; l3=ydim; h3=zdim;
for f=1:CC_volume.NumObjects;

[AllObjects2{1,f}(:,1),AllObjects2{1,f}(:,2),AllObjects2{1,f}(:,3)]=ind2sub([w3,l3,h3],CC_volume.PixelIdxList{1,
f});
end

%Determine where pores lie in terms of depth
for q=1:zdim;
    for p=2:length(AllObjects2);
    junk=find(AllObjects2{1,p}(:,3)==q);
    poresatdepth2(q,p)=length(junk);

    end

end

%Calculate fractional connectivity- the percent of pores at a given depth
%connected to the upper most layer
for g=1:zdim;
    a=find(poresatdepth2(g,:)>0); %Find all pores that traverse through depth q
    totalfrac2(1,g)=length(a);

    [b1,b2]=ind2sub(size(poresatdepth2(g,:)),a);
    fractconn_1=poresatdepth2(:,b2);
    fractconn_2=find(fractconn_1(1,:)>0);%Determine which pores defined above connect to upper layer
    totalfrac2(2,g)=length(fractconn_2);
    totalfrac2(3,g)=totalfrac2(2,g)/totalfrac2(1,g); %Divide pores connected to top by total pores

end

figure; plot(1:zdim,totalfrac2(3,:),'o');

totalfrac2_201405_80_86=totalfrac2;
zdim_201405_80_86=zdim;
```

Create and Plot CDF of Major Axis

```
all_majorax= poresatdepth2;
for n= 2:length(finalSP);
    a=find(all_majorax(:,n)>0);
    %[xa,ya]=ind2sub(a);
    all_majorax(a,n)=(finalSP{1,n-1}(1,:))';
end
```

```
all_majorax2=find(all_majorax);
all_majorax2=all_majorax(all_majorax2);

x_bins_majorax2=1:1:max(round(all_majorax2));
dist_majorax2=hist(all_majorax2,x_bins_majorax2);
dist_majorax2(2,:)=dist_majorax2(1,:)./length(all_majorax2);

for u=2:length(dist_majorax2);
   dist_majorax2(3,1)= dist_majorax2(2,1);
   dist_majorax2(3,u)= dist_majorax2(3,u-1)+dist_majorax2(2,u);
   dist_majorax2(4,1)= dist_majorax2(1,1);
   dist_majorax2(4,u)= dist_majorax2(4,u-1)+dist_majorax2(1,u);
end

x_bins_majax2_201405_80_86= x_bins_majorax2;
dist_majax2_201405_80_86= dist_majorax2;

figure;
plot(x_bins_majorax2,dist_majorax2(3,:));

%save('MajorAxis_201405_80_86.mat','x_bins_majax2_201405_80_86','dist_majax2_201405_80_86');
```

Determine SA and Volume of each object

```
% Construct kernel where we can count the
% number of 6-connected neighbor voxels.
conn6Kernel = zeros([3,3,3]);
conn6Kernel(2,2,1) = 1;
conn6Kernel(1,2,2) = 1;
conn6Kernel(2,1,2) = 1;
conn6Kernel(2,3,2) = 1;
conn6Kernel(3,2,2) = 1;
conn6Kernel(2,2,3) = 1;

% For each voxel, determine how many 6-connected neighbors it has.

sumOfFaces = convn(stackbw3, conn6Kernel, 'same');

% Find number of exposed faces for each voxel. Any 0 pixels will have surfaceArea equal to a negative values.
% If voxel is in center of pore, surfaceArea will equal 0. Any positive
% number an exposed face of the pore.
surfaceArea = 6 * stackbw3 - sumOfFaces;
volume=7 * stackbw3 - sumOfFaces;
% Mask out zero voxels that have negative exposed faces.
% volume=surfaceArea;
% volume(volume >= 0)= 1;
% volume(volume < 0)= 0;
% surfaceArea(surfaceArea<0) = 0;


%%NOTE: for skeletonization, multiply stackbw by 6, not 7. This will set
%%only pixels on the outside of pores to positive numbers!!

% Now we simply label the volume and sum up the values of each region.
% binarySA = surfaceArea > 0;
% ccSA = bwconncomp(binarySA, 6);
% binaryVOL= volume > 0;
```

```
% ccVOL=bwconncomp(binaryVOL,6);

% Now it's labeled, so now we measure the PixelValues in each blob.
measurementsSA = regionprops(CC_volume, surfaceArea, 'PixelValues');
measurementsVOL= regionprops(CC_volume,volume, 'PixelValues');

% Go through the regions, listing each regions exposed surface area.
numberOfRegions = length(measurementsSA);

for k = 1 : numberOfRegions
% For this region, find out the sum of exposed faces.
SAPixelValues = [measurementsSA(k).PixelValues];
% Sum up the number of exposed faces for each voxel in the blob.
SurfaceArea(k,1) = sum(SAPixelValues);
Volume(k,1)=length(measurementsVOL(k).PixelValues); %each voxel measures 1x1x1 pixel
end
```

Calculate SA/V ratio and derive arrays for PDF

```
SAVratio=SurfaceArea3./Volume3;
totalvolume=sum(Volume3);

valuesav=[0:.2:6];
freqsav=histc(SAVratio,valuesav);

numofpores=length(Volume3);
freqsav_pdf=freqsav./numofpores;

for n=2:length(freqsav_pdf)
   freqsav_pdf(n,2)=freqsav_pdf(n,1)+ sum(freqsav_pdf(1:(n-1),1));
end

freqsav_pdf_201405_80_86=freqsav_pdf;

%Calculate as a function of the total brine volume fraction
for n=1:(length(valuesav)-1)
   sav1=find(SAVratio<=valuesav(1,n+1) & SAVratio>valuesav(1,n));
   junkvol=Volume3(sav1);
   portion_of_vol(n,1)=sum(junkvol);
   portion_of_vol(n,2)=portion_of_vol(n,1)/totalvolume;
end

sav1=find(SAVratio>valuesav(1,end));
sav_vol_1=Volume3(sav1);
portion_of_vol(length(valuesav),1)=sum(sav_vol_1);
portion_of_vol(length(valuesav),2)=portion_of_vol(length(valuesav),1)/totalvolume;
```

Create PDF for Mean Pore Volume

```
%valuevol=[0:1e2:max(Volume3)];
valuevol=[0 10 20 50 100 200 500 1e3 2e3 5e3 1e4 2e4 5e4 1e5 2e5 5e5 1e6];
freqvol=histc(Volume3,valuevol);

freqvol_pdf=freqvol/numofpores;

for n=2:length(freqvol_pdf)
   freqvol_pdf(n,2)=freqvol_pdf(n,1)+ sum(freqvol_pdf(1:(n-1),1));
end
```

```
freqvol_pdf_201405_80_86=freqvol_pdf;

%Calculate PDF as function of total brine volume fraction
for n=1:(length(valuevol)-1);
   voljunk=find(Volume3<=valuevol(1,n+1) & Volume3>valuevol(1,n));
   junkvolvol=Volume3(voljunk);
   portion_of_volvol(n,1)=sum(junkvolvol);
   portion_of_volvol(n,2)=portion_of_volvol(n,1)/totalvolume;
end

savjunk_vol_2=find(Volume3>valuevol(1,end));
junkvol_vol_2=Volume3(savjunk_vol_2);
portion_of_volvol(length(valuevol),1)=sum(junkvol_vol_2);
portion_of_volvol(length(valuevol),2)=portion_of_volvol(length(valuevol),1)/totalvolume;

portion_of_vol_201405_80_86= portion_of_vol;
portion_of_volvol_201405_80_86=portion_of_volvol;

%Calculate mean,mode,median for mean pore volume
meanvol_201405_80_86=mean(Volume3);
modevol_201405_80_86=mode(Volume3);
medianvol_201405_80_86=median(Volume3);

%Calculate mean,mode,median for SA/V ratio
meansav_201405_80_86=mean(SAVratio);
modesav_201405_80_86=mode(SAVratio);
mediansav_201405_80_86=median(SAVratio);
```